Acta Materialia 305 (2026) 121835

Contents lists available at ScienceDirect

Acta Materialia

journal homepage: www.elsevier.com/locate/actamat

Revealing the three-dimensional morphology and formation process of Fe-contained intermetallic compounds in aluminum alloys: A combined first-principles, phase field, and FIB-SEM tomography study

Jiale Ma [a,b], Yanli Zhang [a,b], Qing Peng [c], Qingyan Xu [a,b], Haidong Zhao [d], Zhiqiang Han [a,b,*]

[a] School of Materials Science and Engineering, Tsinghua University, Beijing, 100084, China
[b] Key Laboratory for Advanced Materials Processing Technology (Ministry of Education), Tsinghua University, Beijing, 100084, China
[c] School of Power and Mechanical Engineering, Wuhan University, Wuhan, 430072, China
[d] National Engineering Research Center of Near-net-shape Forming for Metallic Materials, South China University of Technology, Guangzhou, 510000, China

ARTICLE INFO

Keywords:
First-principles calculations
Phase field method
Fe-contained intermetallic compounds
Anisotropic interfacial energy
Three-dimensional morphology

ABSTRACT

The three-dimensional morphology and formation process of Fe-contained intermetallic compounds (IMCs), known to impair the mechanical properties of aluminum (Al) alloys, have long remained an unsolved mystery. This lack of fundamental understanding hindered the development of strategies for their morphological control. In this work, the formation process of Fe-contained IMCs in Al alloys was revealed for the first time through a rigorously physics-based approach, combining first-principles/phase field modeling and focused ion beam-scanning electron microscopy (FIB-SEM) tomography. The unique contributions of this research lie in three aspects: First, we performed first-principles calculations to determine the interfacial energies of π-AlFeMgSi, α-AlFeMnSi, and β-AlFeSi phases along multiple crystallographic orientations, and provided a quantitative description for their anisotropic interfacial energies, representing the first report of such fundamental data. Subsequently, the anisotropic interfacial energies were parametrized into phase field models to examine the morphology evolution of Fe-contained IMCs. Two distinct growth modes, free growth in melt and concurrent growth with Al phases, were proposed innovatively, both of which are proved by experiments. Moreover, instead of the widely used X-ray imaging methods, which struggle to differentiate Fe-contained IMCs from other IMCs because of comparable X-ray absorption, FIB-SEM tomography was applied to specifically characterize the three-dimensional morphology of Chinese-script α-AlFeMnSi phases. A novel interpretation for the formation mechanism of this intricate morphology was proposed, which is further elucidated by phase field modeling. This study offered unprecedented insights into the morphology and formation process of Fe-contained IMCs, exploring a way for the rational design of morphology control strategies.

1. Introduction

Aluminum (Al) alloys are extensively utilized in manufacturing transportation equipment due to their excellent specific strength, superior corrosion resistance, and good formability [1,2]. Typically, alloy elements, such as Si and Mg, are deliberately added to Al alloys to improve the strength through solution and precipitation hardening. However, various impurity elements may be introduced into Al alloys during casting processes, particularly Fe. Due to its low solid solubility in Al (~0.05 wt. % [3]), excess Fe tends to react with Al, Si, Mg, and other elements to form brittle, multicomponent intermetallic compounds (IMCs). These Fe-contained IMCs, characterized by high hardness, typically exhibit coarse plate-like, needle-shaped, or blocky morphologies. Acting as stress concentration sites, they significantly deteriorate the mechanical properties of Al alloys, especially ductility [4–6].

It is difficult and uneconomical to remove the Fe form Al melts [7,8]. Consequently, numerous strategies have been explored to modify the type and morphology of Fe-contained IMCs, including the addition of alloying elements (e.g., Mn, Ce, Nd, *Sc*, Cr) [9–16], the optimization of solidification cooling rate [14,17,18] and heat treatment process [19,20], and the application of external fields [21,22]. Among these, the most widely reported control method is Mn additions. This promotes the formation of the α-AlFeMnSi phase, which exhibits a more favorable

* Corresponding author.
E-mail address: zqhan@tsinghua.edu.cn (Z. Han).

https://doi.org/10.1016/j.actamat.2025.121835
Received 12 September 2025; Received in revised form 10 December 2025; Accepted 15 December 2025
Available online 17 December 2025

morphology [23–25]. However, several studies [26–28] have demonstrated that the α-AlFeMnSi phase exhibits higher elastic modulus and microhardness than both β-AlFeSi phase and Al matrix. This makes it more susceptible to stress concentration and facilitates crack initiation. Moreover, excessive Mn additions increase the overall volume fraction of IMCs, further damaging alloy ductility. Consequently, effective control of the morphology of Fe-contained IMCs in Al alloys remains an ongoing challenge.

To effectively modify the morphology of Fe-contained IMCs, fundamental understanding of their three-dimensional (3D) morphology and formation process in Al melts is essential. Terzi et al. [29] employed in situ high-energy synchrotron X-ray microtomography to monitor the nucleation and growth of β-Al_5FeSi plates during solidification of Al-Si casting alloys. Gao et al. [30] used fractographic observations to elucidate the 3D morphologies and growth mechanisms of the α-AlFeMnSi phase in Al alloys. Björnstedt et al. [31] combined X-radiographic imaging with deep-etching techniques to in situ study the morphology and growth kinetics of primary α-Al(Fe, Mn, Cr)Si phases during solidification. Jiao et al. [32] and Wang et al. [33] applied high-resolution synchrotron X-ray tomography to characterize the morphology, clustering behavior, and spatial distribution of α-AlFeMnSi phases in Al alloys, respectively.

Despite numerous publications on this topic providing valuable insights and directions, many unresolved questions remain regarding the formation of Fe-contained IMCs in Al alloys. Specifically, factors like solid-liquid interfacial energies clearly influence morphological evolution during solidification, the precise contributions of these parameters in the formation of Fe-contained IMCs require further clarification. Moreover, techniques like computed tomography and X-ray in situ observation often face challenges in distinguishing Fe-contained IMCs from other IMCs such as AlMn or AlMnSi phases due to their similar X-ray absorption characteristics. Focused ion beam (FIB) and scanning electron microscopy (SEM) tomography (FIB-SEM tomography) enables high-resolution 3D microstructural characterization. Furthermore, signal absorption is not a limiting factor as compared to X-ray based techniques [34]. FIB-SEM tomography has become an important tool in many research areas ranging from characterizing ceramics, metals and alloys [35–37].

Meanwhile, computational modeling and simulation are becoming an indispensable research method for the fields of materials science and engineering. Phase field simulation is a calculation method for simulating the evolution of microstructure [38], which has become a powerful tool for understanding the morphology and formation process of phases [39]. Ning et al. [40] employed a multiphase field model to study the effects of casting temperature and Fe content on the formation of β-$Al_9Fe_2Si_2$ phases. However, they did not systematically describe the morphological characteristics of the Fe-contained IMCs, particularly lacking detailed discussion on the anisotropic interfacial energy used in the model. For crystals, the atomic arrangement varies with crystallographic orientation and defect distribution, which also determines the anisotropy of interfacial energy [41]. Accordingly, the interfacial energy should be expressed as a function of crystal orientation. Previous studies [42,43] have demonstrated that anisotropic interfacial energy significantly influences the evolution of morphologies. Therefore, it is essential to theoretically quantify the anisotropic interfacial energy of crystals and incorporate it into phase field models for more accurate simulations.

Experimentally, it is not feasible to determine solid-liquid interfacial energies for all materials, with only a few exceptions such as transparent organic materials or simple binary alloys [44–46]. Modelling a solid-liquid interface to calculate the interfacial energy is therefore a reasonable alternative. Numerous studies have reported the use of molecular dynamics (MD) simulations to calculate the interfacial energies of systems such as Ni [47], Mg [48], and Al [49]. While MD is well-suited for such calculations, the accuracy of the results heavily depends on suitable interatomic potentials. Unfortunately, for complex ternary and quaternary Fe-contained IMCs systems, appropriate potential functions are currently lacking. First-principles calculations based on Density Functional Theory (DFT) offer a reliable and efficient approach for predicting the stability, electronic structure, and mechanical properties of various intermetallic phases and alloy systems [50]. Unlike MD, DFT does not require empirical interatomic potentials, making it a promising solution to this limitation. Auger et al. [51] successfully employed DFT to calculate the solid-liquid interfacial energies of Fe/Zn, Fe/Pb, and Fe/Bi systems, demonstrating the effectiveness of this approach.

In this paper, a rigorously physics-based simulation framework integrating first-principles calculations with phase field models was established to investigate the 3D morphology and formation processes of Fe-contained IMCs in Al melts. Focusing on three predominant Fe-contained IMCs in Al-Mg-Si alloys: π-AlFeMgSi, α-AlFeMnSi and β-AlFeSi phases, we quantitatively determined their solid (Fe-contained IMCs)-liquid (Al melt) interfacial energies through first-principles calculations. The derived anisotropic interfacial energies were incorporated into phase field models to simulate the morphology and formation process. FIB-SEM tomography and multiphase field modeling were combined to elucidated the formation mechanism of the Chinese-script α-AlFeMnSi phase. The insights gained from this work are expected to provide a theoretical basis for the morphological control and modification of Fe-contained IMCs in Al alloys.

2. Methods

2.1. Calculation of solid-liquid interfacial energy

The computational framework for calculating solid-liquid interfacial energy was illustrated in Fig. 1, integrating DFT, ab initio molecular dynamics (AIMD), and MD simulations.

DFT and AIMD calculations were performed using the Vienna Atomic Simulation Package (VASP v5.4.4) [52,53] with the projector-augmented wave (PAW) pseudopotentials and the Perdew-Burke-Ernzerhof (PBE) generalized gradient approximation (GGA) exchange-correlation functional. For systems containing magnetic elements (Fe and Mn), spin-polarized calculations were conducted with ferromagnetic ordering. The Monkhorst-Pack scheme [54] was systematically applied for Brillouin zone sampling, with k-point meshes adapted to supercell dimensions. Structural relaxations were performed until residual forces on all atoms fell below 0.05 eV/Å. The liquid Al amorphous model at 800 K was generated through MD simulations using the LAMMPS package [55], employing the embedded-atom method (EAM) potential developed by Mendelev et al. [56,57] for interatomic interactions.

The computational procedure comprised the following sequential stages. First, to systematically evaluate the anisotropic interfacial energy between Fe-contained IMCs and Al melts, solid configurations of Fe-contained IMCs with crystallographically distinct surface were established. Subsequent DFT structure optimization was performed using a plane-wave cutoff energy of 350 eV, with the converged total energy recorded as E_{solid}.

Second, the liquid Al structure was established using a supercell filled with Al atoms in periodic boundary conditions. This simplification to pure Al was necessary due to computational constraints: in the actual multicomponent melt (Al-0.8Mg-0.7Si-0.3Fe-0.4Mn), solute atoms (Mg, Si, Fe, Mn) are present in much lower concentrations than Al. To properly include these solute atoms while maintaining realistic concentrations would require a supercell containing hundreds of atoms, which is computationally expensive for the extensive DFT calculations required in this study. The liquid Al models (2.42 g/cm^3 density [58]) were dimensionally matched with expanded Fe-contained IMCs supercells. This geometric coherence ensures atomically continuous interfacial registry while maintaining $<$ 1.0 % lattice mismatch. The MD simulations utilized a 1 fs time step within the NVT ensemble, maintaining the system at 800 K for 3 ps to achieve equilibrium liquid configurations. The final 1 ps Al configuration from MD simulations

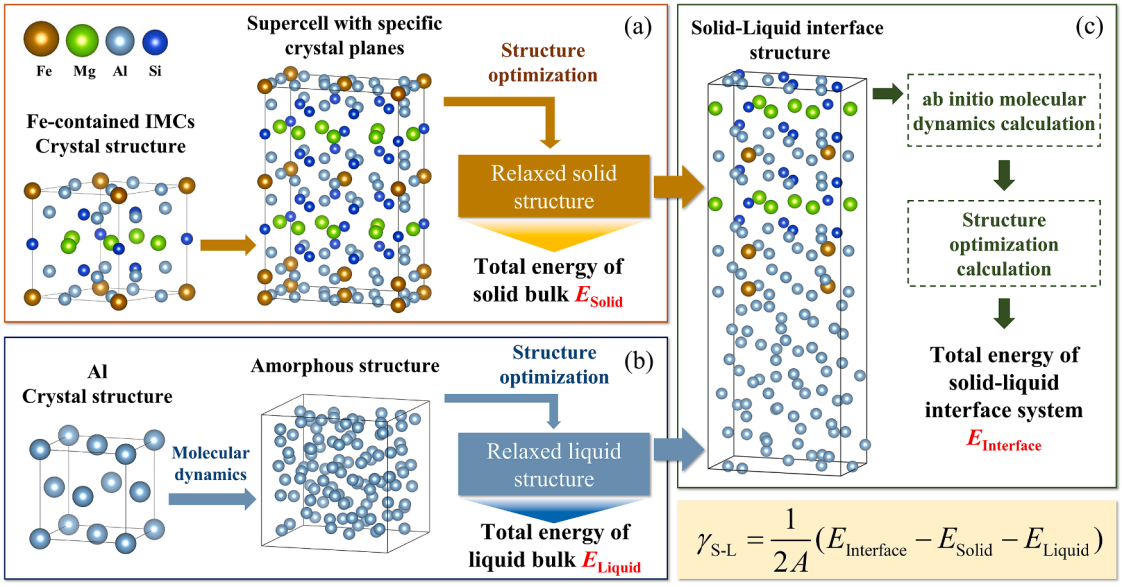

Fig. 1. Schematical illustration of the solid-liquid interfacial energy calculation scheme, which comprises three essential components: (a) construction of the atomic model of the Fe-contained IMCs crystal with specific crystallographic orientations, with subsequent DFT calculation of its total energy; (b) generation of the amorphous Al structure via MD, with subsequent DFT calculation of its total energy; (c) assembly of the relaxed solid and liquid structures into a composite interface structure, followed by AIMD simulation and DFT calculation for the total energy of the solid-liquid system. This integrated approach enables the determination of solid-liquid interfacial energies for specific crystallographic planes of Fe-contained IMCs.

underwent structure optimization calculation using a 2 × 2 × 2 k-point mesh and 350 eV cutoff energy, yielding the relaxed liquid Al structure and liquid phase energy E_{liquid}.

Third, the solid-liquid interface structure was constructed by integrating the relaxed solid and liquid structures into a periodic supercell containing two symmetric solid-liquid interfaces. To preserve the crystallographic integrity of the Fe-contained IMCs while enabling interfacial relaxation, the innermost atomic layers of the solid structure remained fixed during simulations, with the four outermost layers permitted full atomic freedom. AIMD simulations were conducted under the NVT ensemble using the Nosé-Hoover thermostat to maintain system temperature at 800 K. Electronic structure calculations employed a 400 eV plane-wave cutoff energy with Γ-point sampling of the Brillouin zone, achieving energy convergence criteria of 10^{-5} eV. The final 1 ps trajectory was subjected to structure optimization to obtain the relaxed interface configuration and the relaxed interface configuration's total energy $E_{interface}$.

Finally, the solid-liquid interfacial energy was calculated using:

$$\gamma_{S-L} = \frac{1}{2A}\left(E_{interface} - E_{solid} - E_{liquid}\right) \tag{1}$$

where $E_{interface}$, E_{solid}, and E_{liquid} represent the converged total energies of the interface, solid, and liquid structures, respectively. The interfacial area A was determined from the supercell dimensions.

2.2. Phase field models

In phase field models, the phase-state evolution is characterized by a continuous order parameter ϕ, where $\phi = 0$ represents fully melted state, $\phi = 1$ represents fully solidified state, and $0 < \phi < 1$ represents the interfacial region between them. The governing equations for phase evolution and solute transport are formulated as [59,60]:

$$\frac{\partial \phi}{\partial t} = M(\mathbf{n})\left[\nabla\left(\varepsilon^2(\mathbf{n})\nabla\phi\right) + \sum_{u=x,y,z}\left(|\nabla\phi|^2\varepsilon(\mathbf{n})\frac{\partial(\varepsilon(\mathbf{n}))}{\partial(\partial_u\phi)}\right) - wg'(\phi) - h'(\phi)\left(f^S - f^L - \sum_{p=1}^{m}(c_{pS} - c_{pL})\tilde{\mu}_p\right)\right] \tag{2}$$

$$\frac{\partial c_p}{\partial t} = \nabla\cdot(1-h(\phi))\sum_{q=1}^{m} D_{pq}\nabla c_{qL} + \nabla\cdot\left[\frac{\varepsilon_0}{\sqrt{2w}}(c_{pL} - c_{pS})\right]\frac{\partial\phi}{\partial t}\frac{\nabla\phi}{|\nabla\phi|} \tag{3}$$

where D_{pq} is the solute diffusivities, $h(\phi)$ is a monotonous interpolation function and $g(\phi)$ is the double-well potential, which can be found in Eq. (4)(5).

$$h(\phi) = \phi^3\left(10 - 15\phi + \phi^2\right) \tag{4}$$

$$g(\phi) = \phi^2(1-\phi)^2 \tag{5}$$

Here, c_{pS} and c_{pL} are the solute concentration of element p in solid and liquid respectively, which are restricted by the equal chemical potential condition in Eq. (6), where $\tilde{\mu}_p$ is the chemical potential, f^S and f^L are the free energy density of solid and liquid phase. The specific forms of f^S and f^L and their corresponding parameters are given in the Appendix A. For the Fe-contained IMCs systems, their Gibbs free energies were adopted from the work of Du et al. [61–63], in which these IMCs are treated as stoichiometric compounds within the CALculation of PHAse Diagrams (CALPHAD) framework. This treatment assumes fixed compositions for these phases. Consequently, it should be noted that, under this constraint, our model does not account for solute diffusion within the Fe-contained IMCs or across their interfaces.

$$\frac{\partial f^S}{\partial c_{pS}} = \frac{\partial f^L}{\partial c_{pL}} = \tilde{\mu}_p \tag{6}$$

The crystal anisotropy was introduced by taking the gradient energy coefficient $\varepsilon(\boldsymbol{n}) = \varepsilon_0 A(\boldsymbol{n})$ and the phase field mobility $M(\boldsymbol{n}) = M_0 A(\boldsymbol{n})^2$, where $A(\mathbf{n})$ is the anisotropy functional that will be introduced in Section 3.1.4, and $\mathbf{n}$ is the unit normal vector of interface. The isotropic gradient energy coefficient ε_0 and isotropic phase field mobility M_0 is

defined by the following equations [64]:

$$\varepsilon_0 = \sqrt{\frac{6\lambda\gamma_0}{2.2}} \tag{7}$$

$$M_0 = \frac{\gamma_0\sqrt{2w}}{\varepsilon_0^2}\frac{1}{\sum_{p=1}^{m}\frac{\xi_p}{D_p}} \tag{8}$$

$$\xi_p = \frac{RT}{V_M}\left(c_{pL}^e - c_{pS}^e\right)^2 \int_0^1 \frac{h(\phi)(1-h(\phi))}{\left[(1-h(\phi))c_{pL}^e\left(1-c_{pL}^e\right)+h(\phi)c_{pS}^e\left(1-c_{pS}^e\right)\right]\phi(1-\phi)}d\phi \tag{9}$$

where R is the ideal gas constant, T is the temperature, λ is half the thickness of the interface, V_M is the molar volume of the phase, c_{pS}^e and c_{pL}^e are equilibrium solute concentration in solid and liquid respectively, γ_0 is the isotropic interfacial energy and w is the height of the parabolic potential.

$$w = \frac{6.6\gamma_0}{\lambda} \tag{10}$$

In the multiphase field framework, each bulk phase is uniquely identified by its corresponding phase field variable ϕ_i, where $\phi_i = 1$ within the i th phase domain and $\phi_i = 0$ in all other spatial regions. The interfacial transition between adjacent phases is implicitly described through the continuous spatial variation of ϕ_i and ϕ_j, satisfying the conserved phase constraint:

$$\sum_{i=1}^{n}\phi_i = 1 \tag{11}$$

The present work adopted the Kim-Kim-Suzuki-Miodownik (KKSM) multiphase field model developed by Kim et al. [65]. The governing equations are formulated as:

$$\frac{\partial\phi_i}{\partial t} = -\frac{2}{k}\sum_{j\neq i}^{n} s_{ij}M_{ij}(\mathbf{n})\left(\frac{\delta F}{\delta\phi_i}-\frac{\delta F}{\delta\phi_j}\right) \tag{12}$$

$$\frac{\delta F}{\delta\phi_i} = \sum_{j\neq i}^{n}\left[\frac{\varepsilon_{ij}^2(\mathbf{n})}{2}\nabla^2\phi_j + w_{ij}\phi_j\right] + f^i(c) - \sum_{p=1}^{m}\left(c_{ip}\tilde{\mu}_p\right) \tag{13}$$

where n is the total number of coexisting phases in the system, k is the number of coexisting phases at a given spatial coordinate, and s_{ij} is a variable correlated with the number of interfaces in a given domain.

2.3. Experimental procedures

High-purity Al (99.99 %), Al-10Mg, Al-50Si, Al-10Fe and Al-10Mn master alloy were melted in a clay-graphite crucible. The melt was heated to 750 °C and maintained for 2–3 h for homogenization. Then, the melt was poured into a metal mold at the temperature of 700 °C, solidifying at a cooling rate of 3.8 °C/s. The alloy compositions of the solidified alloys were analyzed by an optical emission spectrometer (Optima 3000XLICP) and the average values are listed in Table 1.

3D reconstructions of Fe-contained IMCs were performed using a FIB-SEM dual-beam system (Helios 5 CX), integrating a gallium-based ion beam column, field emission SEM column, and energy-dispersive spectrometer (EDS). Prior to milling, a protective Pt layer was deposited via electron beam-induced deposition over the region of interest (ROI) to prevent ion-induced damage. To optimize imaging conditions for the in-lens secondary electron detector, rectangular trenches were milled: one preceding the ROI and two flanking its lateral sides. Sequential sectioning was conducted at 100 nm increments using the ion beam, with each newly exposed surface imaged by SEM following each milling step. The resulting image stack was automatically compiled into a TIFF format series. Then, this dataset was reconstructed into a 15 × 15 × 10 μm³ volume at 100 nm inter-slice resolution, enabling subsequent 3D visualization.

Table 1
Chemical composition of the studied alloy (wt. %).

Alloy	Mg	Si	Fe	Mn	Al
Al-Mg-Si-Fe-Mn	0.933	0.778	0.332	0.419	Bal.

3. Results and discussion

3.1. Solid-liquid interfacial energy of Fe-contained IMCs

3.1.1. Crystallographic modeling of Fe-contained IMCs

The accurate modeling of crystal structures for Fe-contained IMCs serves as a critical prerequisite for reliable first-principles computational investigations. With the difference of alloy compositions and the presence of crystal defects, Fe-contained IMCs exhibit various crystal structures and stoichiometric ratios. Although their symmetry and crystal structure remain subjects of ongoing debate, these aspects fall beyond the scope of the current study. This work specifically addresses three well-defined π-AlFeMgSi, α-AlFeMnSi, and β-AlFeSi phases with fixed stoichiometric ratios. Their atomic configurations have been rigorously modeled based on advanced structural characterizations and computational modeling in prior studies [66,71–73], as illustrated in Fig. 2.

For the π-AlFeMgSi phase, the hexagonal structure (space group $P\bar{6}2m$, composition $Al_9FeMg_3Si_5$) proposed by Xi et al. [66] was adopted. This configuration (Fig. 2(a)) was rigorously validated through advanced electron microscopy experiments and DFT calculations, confirming its thermodynamic stability and lattice parameter consistency.

The α-AlFeMnSi phase was recognized to originate from the AlMnSi system through substantial substitution of Mn by Fe atoms, resulting in variable Fe/Mn atomic ratios within the phase [67–69]. Dinsdale et al. [70] demonstrated that Fe and Mn exhibit a strong tendency to occupy identical crystallographic sites, driven by a negative mixing enthalpy relative to pure intermetallic constituents. Based on this framework, Zhang et al. [71,72] systematically investigated crystal structures of α-AlFeMnSi with varying Mn/Fe atomic ratios using DFT calculations. Their work identified the thermodynamically most stable configuration (space group $Pm\bar{3}$, composition $Al_{92}Fe_5Mn_{20}Si_{21}$), showing in Fig. 2(b).

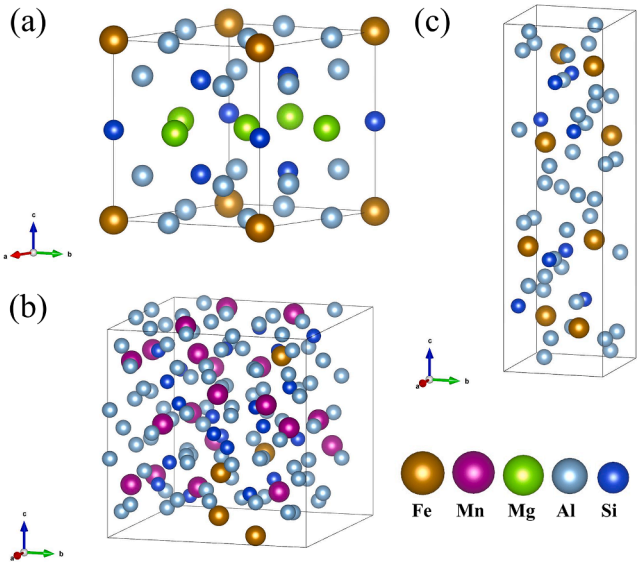

Fig. 2. Crystal structure of (a) π-AlFeMgSi, (b) α-AlFeMnSi, and (c) β-AlFeSi.

For the β-AlFeSi phase, Fang et al. [73] systematically investigated atomic configurations through first-principles calculations, based on experimentally derived models of homogeneous Si/Al atomic distributions [74–76]. By computationally substituting Al atoms with Si at distinct crystallographic sites, they identified the thermodynamically stable monoclinic structure (space group C2/c, composition $Al_{36}Fe_8Si_8$), as shown in Fig. 2(c).

Prior to interfacial modeling, systematic crystallographic operations were performed. Targeted crystallographic planes of the Fe-contained IMCs were cleaved along specific orientations using the surface builder module in VESTA. To ensure lattice compatibility with molten Al systems, the original hexagonal unit cell (π-AlFeMgSi phase) and monoclinic unit cell (β-AlFeSi phase) were transformed into orthogonal supercells via basis vector redefinition, maintaining angular deviations below 1° Subsequent supercell expansions yielded periodic configurations containing 90–120 atoms.

3.1.2. Liquid structure

The investigation of liquid Al structure was performed using equilibrium configurations extracted from the stable regime of MD simulations. To validate the atomic arrangement realism in the simulated liquid phase, the pair correlation function, a fundamental metric describing the probability density of finding atom pairs separated by distance r, was calculated from MD trajectory data. The pair correlation function is mathematically defined for an N-atom system as:

$$\rho_0 g(r) = \frac{1}{N}\left\langle \sum_i \sum_j \delta\left(r - |r_i - r_j|\right) \right\rangle \tag{14}$$

where ρ_0 denotes the average number density, and the Dirac delta function $\delta\left(r - |r_i - r_j|\right)$ counts atomic pairs separated by distance r.

As shown in Fig. 3, the simulated pair correlation function exhibits good agreement with experimental X-ray diffraction data [77,78]. This quantitative match confirms the fidelity of the MD derived liquid configurations for subsequent interfacial modeling.

3.1.3. Solid-liquid interface structure

The analysis of solid-liquid interface structures was conducted using equilibrium configurations derived from AIMD simulations. Fig. 4 presents the time-averaged atomic positions and projected atomic-density profiles along the interface normal direction for π-AlFeMgSi(0001)/Al, α-AlFeMnSi(001)/Al, and β-AlFeSi(001)/Al systems. The projected atomic-density profile $\rho(z)$ calculated as:

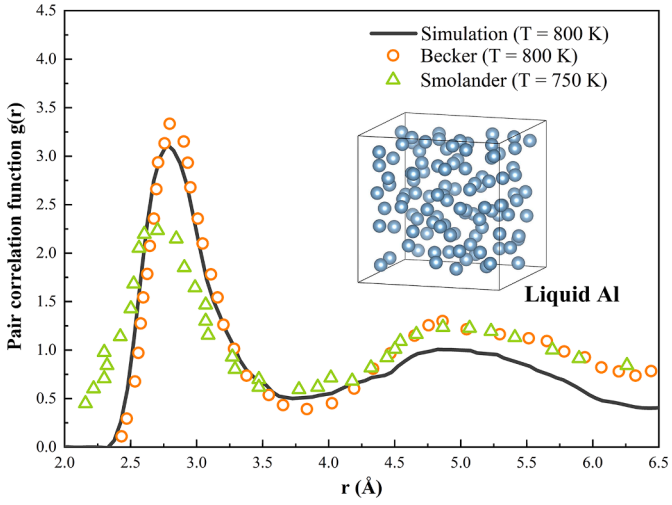

Fig. 3. Pair correlation function $g(r)$ for liquid Al obtained from MD simulations, and the experimental X-ray diffraction data. The atomic configuration of the simulated amorphous Al structure is shown in the inset.

$$\rho(z) = \frac{\langle N_z \rangle}{L_x L_y \Delta z} \tag{15}$$

where $\langle N_z \rangle$ is the time average of the number of particles between z and $z+\Delta z$. L_x and L_y are lateral sizes of the simulation box.

The projected atomic-density profiles reveal distinct structural signatures across the solid-liquid interface. Sharp density maxima on the solid-phase side arise from the fixed lattice positions of crystalline atoms, while the liquid region exhibits characteristic density fluctuations that maintain symmetry due to the periodic boundary conditions. Interfacial analysis shows pronounced atomic layering in the liquid phase extending over 3–4 atomic layers near the interface, with spatial decay following an exponential relationship. This layering consistent with atomistic simulations of solid-liquid interfaces, demonstrates a progressive structural transition from a statistically averaged ordered configuration near the solid surface to a fully disordered liquid structure in the bulk region.

3.1.4. The function of anisotropic interfacial energy

The anisotropy of solid-liquid interfacial energies was quantified through spherical harmonic expansions, incorporating crystallographic symmetry constraints. For the hexagonal π-AlFeMgSi phase, the anisotropy function follows Sun et al.'s formulation [79] utilizing linear combinations of spherical harmonics y_{20}, y_{60}, and y_{66} (Eq. (16)). The anisotropy of Cubic α-AlFeMnSi adopts Fehlner et al.'s model [80] based on cubic harmonic functions (Eq. (17)). For monoclinic β-AlFeSi, we developed a novel function through linear interpolation of y_{20} and y_{22} harmonics (Eq. (18)). Here θ and φ denote the polar and azimuthal angles in spherical coordinates, respectively.

$$\gamma_{\pi-\mathrm{AlFeMgSi}}(\theta,\varphi) = \gamma_0\left(1 + \varepsilon_{20}y_{20} + \varepsilon_{60}y_{60} + \varepsilon_{66}y_{66}\right) \tag{16}$$

$$\gamma_{\alpha-\mathrm{AlFeMnSi}}(\theta,\varphi) = \gamma_0\left(1 + \alpha_1 K_1 + \alpha_2 K_2\right) \tag{17}$$

$$\gamma_{\beta-\mathrm{AlFeSi}}(\theta,\varphi) = \gamma_0\left(1 + \varepsilon_{20}y_{20} + \varepsilon_{22}y_{22}\right) \tag{18}$$

$$y_{20} = \sqrt{\frac{5}{16\pi}}\left(3\cos^2\theta - 1\right) \tag{19}$$

$$y_{22} = \sqrt{\frac{15}{32\pi}}\left(\sin^2\theta sin(2\varphi)\right) \tag{20}$$

$$y_{60} = \frac{\sqrt{13}}{32\sqrt{\pi}}\left(231\cos^6\theta - 315\cos^4\theta + 105\cos^2\theta - 5\right) \tag{21}$$

$$y_{66} = \frac{\sqrt{6006}}{64\sqrt{\pi}}\sin^6\theta\cos(6\varphi) \tag{22}$$

$$K_1 = \sin^4\theta\left(cos^4\varphi + \sin^4\varphi\right) + cos^4\theta - \frac{3}{5} \tag{23}$$

$$K_2 = 3\left(\sin^4\theta\left(cos^4\varphi + \sin^4\varphi\right) + cos^4\theta\right) + 66\sin^4\theta cos^2\theta\sin^2\varphi cos^2\varphi - \frac{17}{7} \tag{24}$$

The first-principles calculated interfacial energies and corresponding crystallographic orientations, shown in Table 2, were parametrized within these functions to determine associated anisotropy parameters. The values of the isotropic interfacial energies and associated anisotropy parameters were given in Table 3.

The Wulff theorem [81] not only states that the equilibrium shape of a macroscopic crystal with a given volume is determined by the surface energy or interfacial energy as a function of crystallographic orientation, but also provides a method for constructing this equilibrium geometry. According to the theorem, the normal vector of each crystal facet can be drawn from the center of symmetry, with its length proportional to the

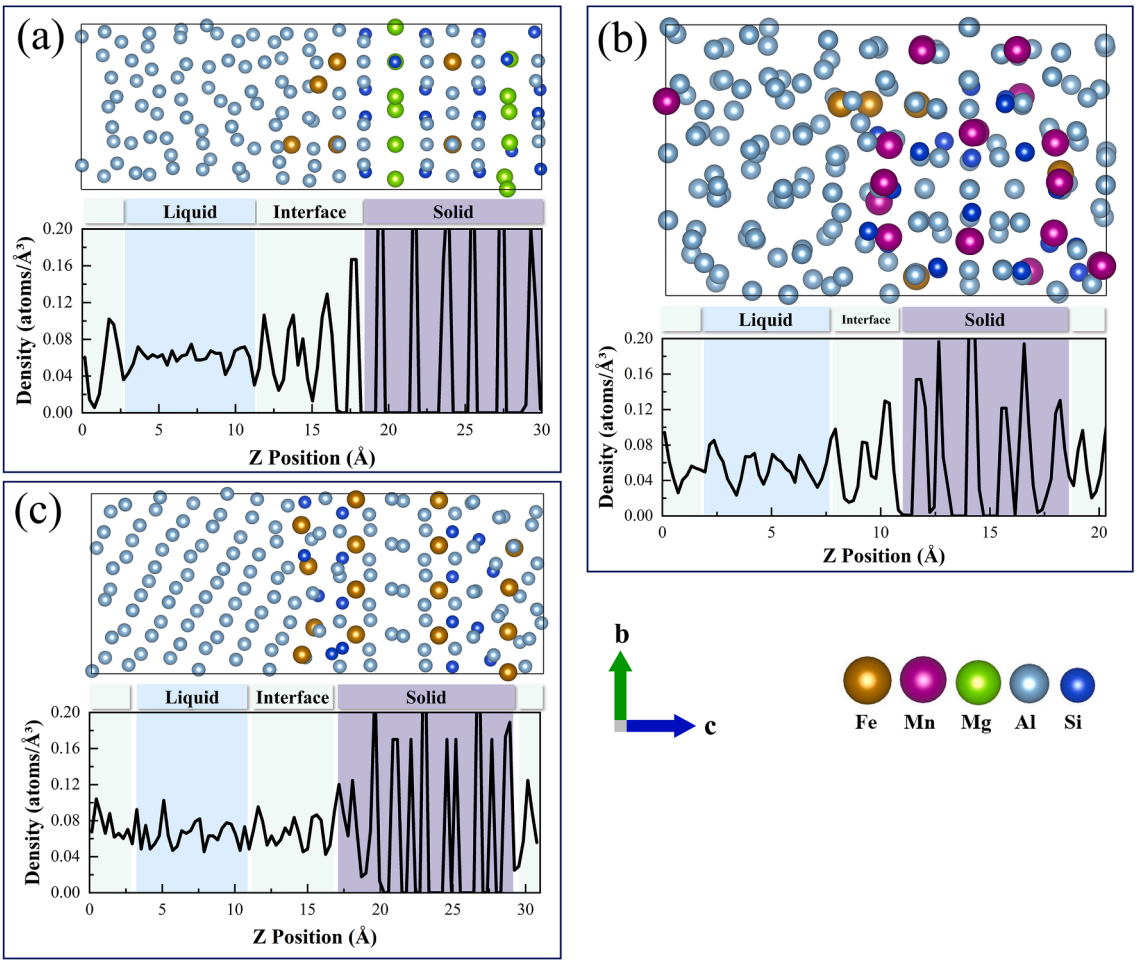

Fig. 4. Diagrams of average atomic position of interface at 800 K and projected atomic-density profile of (a) π-AlFeMgSi(0001)/Al; (b) α-AlFeMnSi(001)/Al; (c) β-AlFeSi(001)/Al.

Table 2
Interfacial energies for different crystalline orientations of Fe-contained IMCs.

Phase	Crystal plane	Interfacial energy (J/m^2)
π-AlFeMgSi	(0001)	0.359
	(11$\bar{2}$1)	0.602
	(10$\bar{1}$1)	0.667
	(10$\bar{1}$0)	0.543
α-AlFeMnSi	(001)	0.450
	(110)	0.386
	(111)	0.817
β-AlFeSi	(001)	3.955
	(110)	1.984
	(111)	2.998

Table 3
Isotropic interfacial energies and associated anisotropy parameters of Fe-contained IMCs.

Phase	γ_0 (J/m^2)	Anisotropy parameters		
π-AlFeMgSi	0.642	ε_{20} 0.159	ε_{60} −0.531	ε_{66} 0.399
α-AlFeMnSi	0.516	α_1 −0.835	α_2 0.361	
β-AlFeSi	3.455	ε_{20} 0.229	ε_{22} −0.915	

interfacial energy of the corresponding crystal plane. The resulting equilibrium morphology, known as the Wulff shape, reflects the anisotropy of interfacial energy and represents the crystal shape in the absence of volume strain energy and homogeneous nucleation. Based on this, the equilibrium shapes of three Fe-contained IMCs were obtained, as shown in Fig. 5.

3.2. Phase field simulation for the Fe-contained IMCs

3.2.1. Phase field simulation for the free growth of Fe-contained IMCs

The solidification pathway of Al-0.8Mg-0.7Si-0.3Fe-0.4Mn alloy was calculated using Thermo-Calc® with the Scheil-Gulliver model, with results presented in Fig. 6. The calculated Fe-contained IMCs in this alloy include $Al_{15}(Fe, Mn)_4Si_2$ (α-AlFeMnSi), Al_8Fe_2Si and $Al_9Fe_2Si_2$ (β-AlFeSi), and $Al_{18}Fe_2Mg_7Si_{10}$ (π-AlFeMgSi), which are consistent with the targeted phases investigated in this study. The formation temperatures of these Fe-contained IMCs obtained from Scheil-Gulliver simulations were utilized as initial temperatures for the phase field modeling. Thermodynamic data (e.g., equilibrium concentrations) and kinetic parameters (e.g., diffusion coefficients) were obtained from Thermo-Calc®. The simulation domain measured 125 × 125 × 125 grid points with a uniform grid spacing of $\Delta x = 0.6$ μm.

In general, the final morphology of a crystal is governed by both intrinsic crystallographic characteristics (e.g., anisotropic interfacial energy) and extrinsic factors from the surrounding environment (e.g., the presence of α-Al dendrites). The intrinsic factors tend to drive the phase toward equilibrium crystal shapes that minimize the total

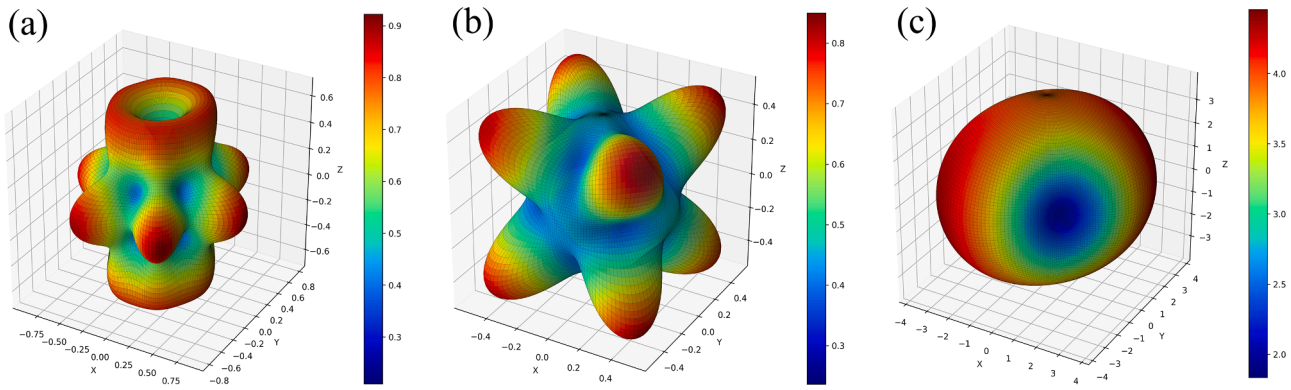

Fig. 5. Wulff structures of (a) π-AlFeMgSi; (b) α-AlFeMnSi; (c) β-AlFeSi.

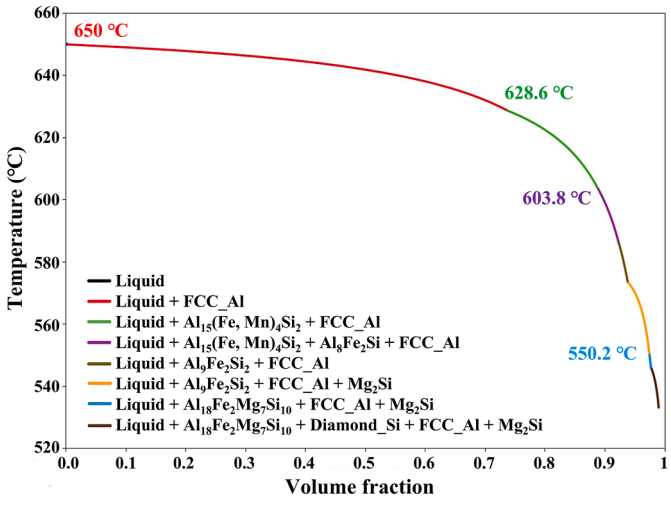

Fig. 6. The solidification sequence of Al-0.8Mg-0.7Si-0.3Fe-0.4Mn alloy in Scheil model.

interfacial free energy. However, external influences often disrupt this equilibrium, resulting in deviations in size and morphology. To investigate the intrinsic crystallographic morphology of Fe-contained IMCs in isolation, all external environmental influences were deliberately excluded, allowing the phases to grow freely in a homogeneous liquid matrix. Accordingly, the simulation was initiated by introducing a single solid seed with a radius of $R_0 = 3.0$ μm at the center of the computational domain.

Fig. 7 presents the simulated 3D morphology of Fe-contained IMCs and their corresponding cross-sectional views. Fig. 7(a1) shows the results of the π-AlFeMgSi phase, which exhibits a faceted, convex hexagonal prism-like morphology. The preferred growth directions lie along the $\langle 10\bar{1}1\rangle$, $\langle 10\bar{1}0\rangle$, and $\langle 10\bar{1}\bar{1}\rangle$ crystallographic families. Scheil model predictions (Fig. 6) indicate that the π-AlFeMgSi phase only nucleates at a very late stage of solidification, when the remaining liquid fraction falls below 5 %. Consequently, during actual solidification processes of Al-0.8Mg-0.7Si-0.3Fe-0.4Mn alloys, π-AlFeMgSi phases inevitably become constrained by surrounding α-Al dendrites or other intermetallic phases, which disrupts the equilibrium morphology. Moreover, no experimental work has documented a clear, characteristic shape for π-AlFeMgSi phases [82–84], so there are currently no suitable data in the literature and our experiments to validate the simulated equilibrium morphology for π-AlFeMgSi phase.

Fig. 7(b1) shows the simulated morphology of the α-AlFeMnSi phase, which exhibits a perfect rhombic dodecahedral shape. The crystal grows preferentially along the $\langle 100\rangle$ and $\langle 111\rangle$ directions, with {110} facets forming under faceted growth kinetics. This simulation agrees well with numerous experimental observations [30,33,71,72,85–87].

The β-AlFeSi phase is widely recognized to possess a characteristic needle, plate-like morphology [29,85,87]. As shown in Fig. 7(c1), the simulated β-AlFeSi exhibits a convex, lens-shaped geometry, with preferred growth directions along $[1\bar{1}0]$, $[\bar{1}10]$, [001] and $[00\bar{1}]$ et al., in agreement with the experimental observations.

3.2.2. *Multiphase field simulation for the concurrent growth of α-Al and Fe-contained IMCs*

Thermodynamic analysis (Fig. 6) reveals that the Fe-contained IMCs nucleate after extensive growth of α-Al dendrites. As the primary α-Al dendrites solidify, they partition solute elements like Fe into the inter-dendritic liquid, enabling the local supersaturation necessary for IMCs formation. Research [88] also shows that Fe-contained IMCs preferentially nucleate on or near primary α-Al dendrites. Under such heterogeneous nucleation conditions, the Fe-contained IMCs and the α-Al phase grow concurrently from the liquid. Due to the presence of the pre-existing α-Al solid and the difference in anisotropic growth rates (Fe-contained IMCs and Al phases), the growth of the Fe-contained IMCs along certain directions will be strongly confined, preventing the development of their thermodynamically equilibrium morphology. This growth behavior is defined here as 'concurrent growth'.

To elucidate this concurrent growth behavior, we implemented multiphase field models in which the primary α-Al dendrites were represented as a planar substrate and Fe-contained IMCs were nucleated on its surface, as shown in Fig. 8(a1)-(a3). For the π-AlFeMgSi phase (Fig. 8 (b1)-(b3)), simulations along the $[10\bar{1}0]$ and [0001] directions shown that lateral growth against the Al phase is severely restricted. The growth is thus confined to the direction normal to the substrate, producing elongated, rod-like morphology.

The α-AlFeMnSi phase (Fig. 8(c1)-(c3)) also exhibits a distinct growth pattern. Along its preferred growth directions $\langle 001\rangle$ and $\langle 111\rangle$, the α-AlFeMnSi phase grows faster than the Al phases, while slower-growing orientations become overgrown by Al phases, forming hollow quadrilateral pyramid structures. Continued concurrent growth along the [001] direction (perpendicular to the substrate) transforms the α-AlFeMnSi phase into skeletal tetragonal prism structures.

Such skeletal morphologies have been observed in experimental studies [30,31,33], where the skeletal morphologies were interpreted as transitional forms preceding rhombic dodecahedron development. However, this work reveals that they actually represent distinct growth modes, as illustrated in Fig. 9(b). When freely growing in the liquid phase, α-AlFeMnSi develops a perfect dodecahedral morphology driven by anisotropic interfacial energy. However, during concurrent growth with Al phases, lateral expansion becomes constrained, forcing growth perpendicular to the solid-liquid interface. This results in a rod shaped skeletal tetragonal morphology. Specifically, our proposed growth sequence involves: (1) nucleation on the α-Al dendrites, (2) formation of

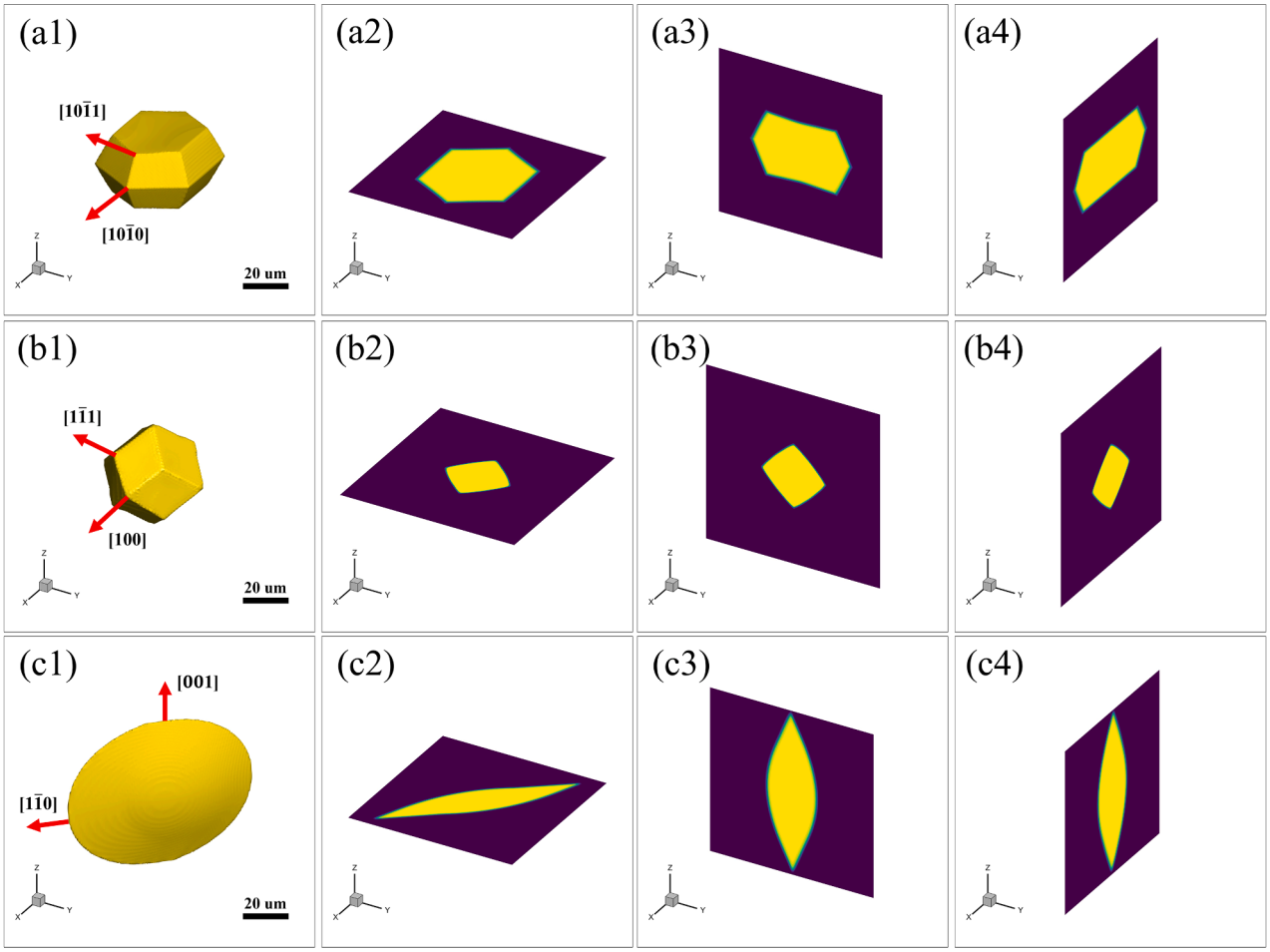

Fig. 7. Simulation results of 3D morphology for (a1) π-AlFeMgSi phase, (b1) α-AlFeMnSi phase, and (c1) β-AlFeSi phase and corresponding cross-sectional views: (a2) (b2) (c2) XY-plane projections; (a3) (b3) (c3) ZY-plane projections; (a4) (b4) (c4) ZX-plane projections.

hollow quadrilateral pyramids through concurrent growth with Al phases, and (3) vertical layer-by-layer growth yielding rod-shaped skeletal tetragonal pyramids morphology.

In contrast, the β-AlFeSi phase (Fig. 8(d1)-(d3)) rapidly extends along its preferred orientations with minimal substrate influence. As a result, β-AlFeSi consistently display a platelet-like morphology.

Overall, the phase field models accurately capture the thermodynamics and kinetics of Fe-contained IMCs during free growth in liquid and concurrent growth with Al phases. This new insight contributes to understand the diverse morphological manifestations of Fe-contained IMCs in Al alloys, attributing them to different local solidification environments rather than a single, time-dependent evolutionary path.

3.3. 3D characterization of the Fe-contained IMCs

Beyond the two aforementioned distinct morphologies of α-AlFeMnSi phases, the well-known Chinese-script morphology also represents another significant form. To elucidate the 3D morphology of the complex Chinese-script α-AlFeMnSi phase, FIB-SEM tomography was employed for characterization.

A Chinese-script structured phase was initially selected for analysis. Its composition was determined via EDS, confirming identification as α-AlFeMnSi phase (Fig. 10(a1)-(a6)). Prior to milling, a Pt protective layer was deposited over the phase surface. Rectangular trenches were then milled around the ROI using a focused Ga ion beam, exposing the target area (Fig. 10(b1)). As shown in Fig. 10(b2)(b3), sequential material removal and electron beam imaging were subsequently performed iteratively.

The reconstructed 3D morphology of the Chinese-script α-AlFeMnSi phase was shown in Fig. 10(c1), where the Al matrix has been omitted for visual clarity. The α-AlFeMnSi phase consists of several distorted plate-like structures connected by nodes between the plates (Fig. 10(c2)(c3)). Some studies [32,33] proposed that primary compressed α-AlFeMnSi phases gradually develop into dendritic forms that interconnect to form Chinese-script morphologies. However, in the 3D reconstruction of the Chinese-script α-AlFeMnSi phase, we did not observe any rhombic dodecahedral cores at the center of the structures. Consequently, we proposed that the Chinese-script α-AlFeMnSi phase do not evolve spontaneously from primary rhombic dodecahedral phases, but rather forms through distinct mechanisms.

3.4. The formation mechanism for Chinese-script α-AlFeMnSi phase

Controversy persists regarding the formation mechanism of the Chinese-script α-AlFeMnSi phase, with some studies [32,33] proposing that the Chinese-script α-AlFeMnSi phase is formed from the compacted primary α-AlFeMnSi phase. However, recent evidence [89,90] have suggested that the Chinese-script morphology develops from the concurrent growth of the Fe-contained phase with the Al phases.

In this study, 3D multiphase field models were employed to replicate the formation process of Chinese-script α-AlFeMnSi phase and elucidate its underlying mechanisms. With α-Al dendrites modeled as a planar substrate, α-AlFeMnSi phases nucleate on the dendrite surface and, together with the Al phases, grow perpendicular to the solid-liquid

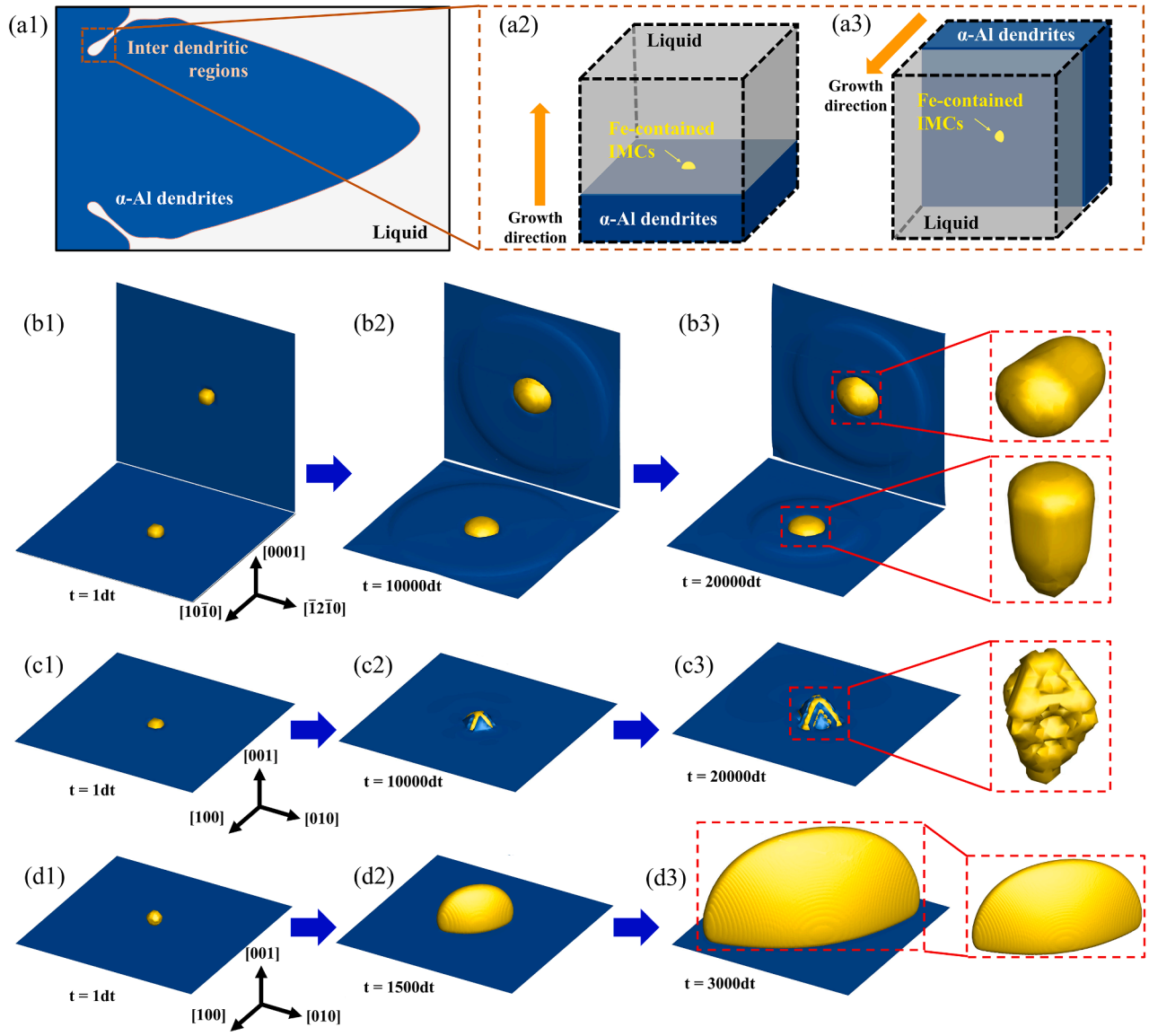

Fig. 8. (a1)-(a3) Schematical illustration of spatial position and growth direction of Fe-contained IMCs. The size of the computational domain (black dashed box) is 60×60×60 μm^3. The simulation results for the concurrent growth of Al phases (blue) and Fe-contained IMCs (yellow): (b1)-(b3) π-AlFeMgSi phase; (c1)-(c3) α-AlFeMnSi phase; (d1)-(d3) β-AlFeSi phase.

interface along the [100], [010], and [001] crystallographic directions (Fig. 11(a)). For clarity in visualizing the morphological evolution of the α-AlFeMnSi phases, the Al phase is not displayed in the subsequent simulation results (Fig. 11(b1-b6)). However, it should be noted that the Al phases continue to grow concurrently throughout the simulated process. At 10,000-time steps (Fig. 11(b3)) and 15,000-time steps (Fig. 11(b4)), adjacent rod-like α-AlFeMnSi phases coalesce laterally (red dashed circle). Subsequent evolution shows interconnection between [001]-oriented and [100]-oriented α-AlFeMnSi phases at 20,000 steps. By 25,000 steps, these connected α-AlFeMnSi phases integrate into a unified netlike structure. In addition, Al phases (blue regions) progressively encroach upon the α-AlFeMnSi during growth (Fig. 11(c)), imposing geometric confinement that restricts further growth. This growth pattern ultimately yields the characteristic convoluted morphology of Chinese-script α-AlFeMnSi phases.

Furthermore, 2D slices of the multiphase field simulations and FIB-SEM tomography results were presented in Fig. 11(d)(e). The 3D morphologies of Chinese-script α-AlFeMnSi phases obtained from simulations and experiments consistently exhibit curled lamellar structures, while the corresponding 2D cross-sections display complex Chinese-script patterns. In the current multiphase field model, α-AlFeMnSi nuclei were deliberately assigned perpendicular growth directions for computational simplicity. However, during actual solidification processes, the spatial arrangement of α-Al dendrites creates more complex environments. When α-AlFeMnSi phases nucleate on these irregular dendritic surfaces or in the liquid, their growth orientations become considerably more varied. This results in the formation of interconnected plate-like structures with significantly greater morphological irregularity compared to the simulations. Qualitatively speaking, the multiphase field model and formation mechanism proposed in this study successfully replicate and explain the fundamental formation process of Chinese-script α-AlFeMnSi phases. This work establishes a scientific foundation for more comprehensive quantitative investigations in future research.

4. Conclusions

In the present work, multi-scale first-principles/phase field modeling

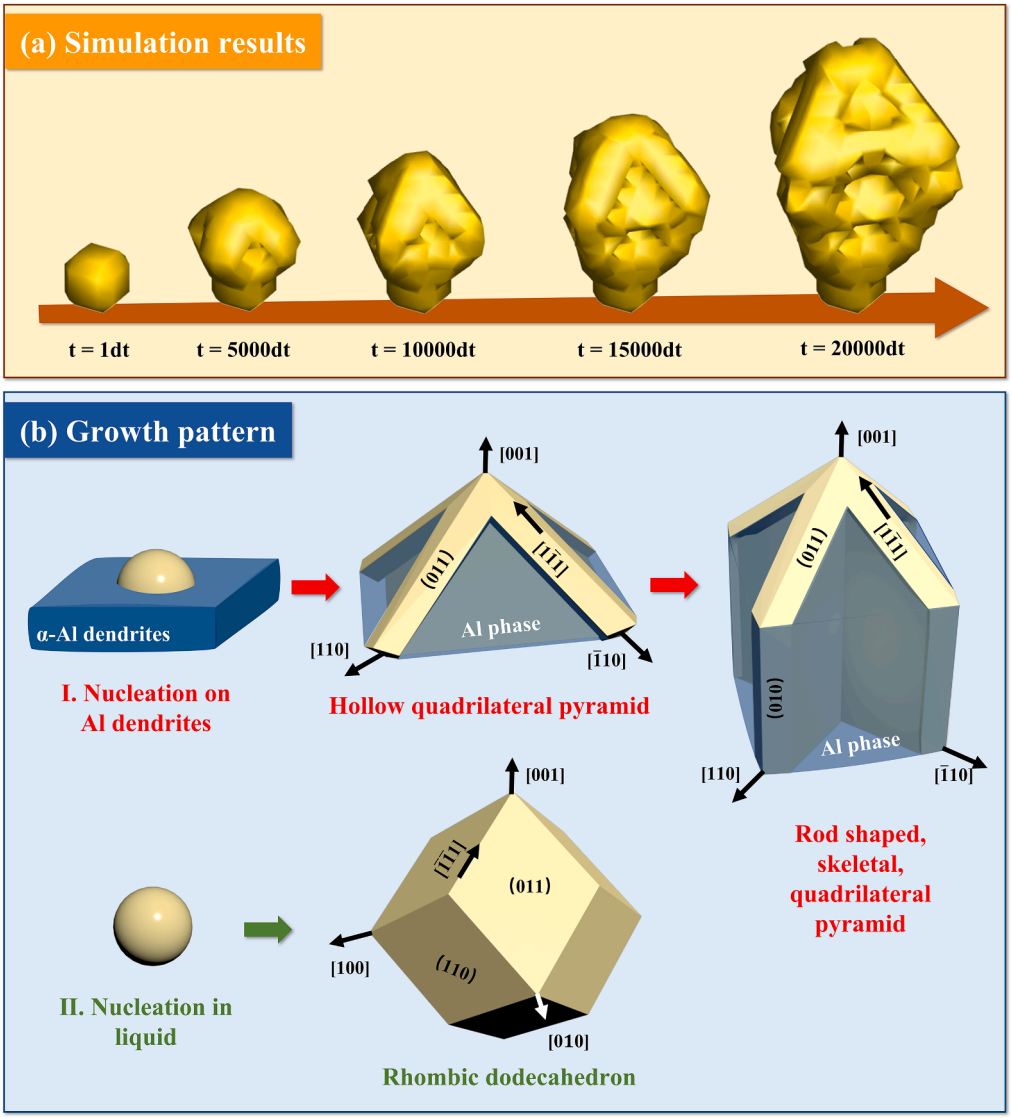

Fig. 9. Phase field simulation results and schematic illustration of the growth patterns of the α-AlFeMnSi phase: (a) morphological evolution captured at different time steps; (b) schematic diagram elucidating the two growth modes: mode I, where the phase nucleates on α-Al dendrites and develops via concurrent growth with Al phases; mode II, where it nucleates freely within the melt and grows independently.

combined with FIB-SEM tomography were conducted to investigate the 3D morphology and formation process of Fe-contained IMCs in Al alloys. The main conclusions are summarized as follows:

(1) Employing first-principles calculations, this study pioneered the determination of solid-liquid interfacial energies for π-AlFeMgSi, α-AlFeMnSi, and β-AlFeSi phases across key crystallographic orientations, including (0001), (11$\bar{2}$1), (10$\bar{1}$1), and (10$\bar{1}$0) for π-AlFeMgSi/Al system and (001), (110), and (111) for α-AlFeMnSi/Al and β-AlFeSi/Al systems. These efforts yielded quantitative models capturing the orientation-dependent interfacial energy behavior of Fe-contained IMCs, formulated as follows:

$$\gamma_{\pi-\mathrm{AlFeMgSi}}(\theta,\varphi) = 0.642\left(1+0.159y_{20}-0.531y_{60}+0.399y_{66}\right)$$

$$\gamma_{\alpha-\mathrm{AlFeMnSi}}(\theta,\varphi) = 0.516(1-0.835K_1+0.361K_2)$$

$$\gamma_{\beta-\mathrm{AlFeSi}}(\theta,\varphi) = 3.455\left(1+0.229y_{20}-0.915y_{22}\right)$$

(2) Phase field models incorporating the derived anisotropic interfacial energies were developed to simulate the morphology evolution of the Fe-contained IMCs. By varying the nucleation sites, both free growth in liquid and concurrent growth with Al phases of the Fe-contained IMCs were modeled, revealing their preferential growth directions and resulting morphologies under different growth conditions. In particular, the α-AlFeMnSi phase exhibits two unique morphologies: the rhombic dodecahedron structure under free growth conditions and the rod-shaped skeletal tetragonal pyramid under concurrent growth conditions. These findings provide new insights that challenge previous assumptions regarding the formation process of α-AlFeMnSi phase and are proved by experimental evidence.

(3) FIB-SEM tomography was applied to specifically characterize the Chinese-script α-AlFeMnSi phase. Compositional analysis via EDS confirmed the identity of the selected phase, and 3D reconstruction uncovered an interconnected network of distorted, plate-like structures. The formation mechanism of its intricate morphology was further revealed via multiphase field simulations, demonstrating that the Chinese-script morphology originates from the

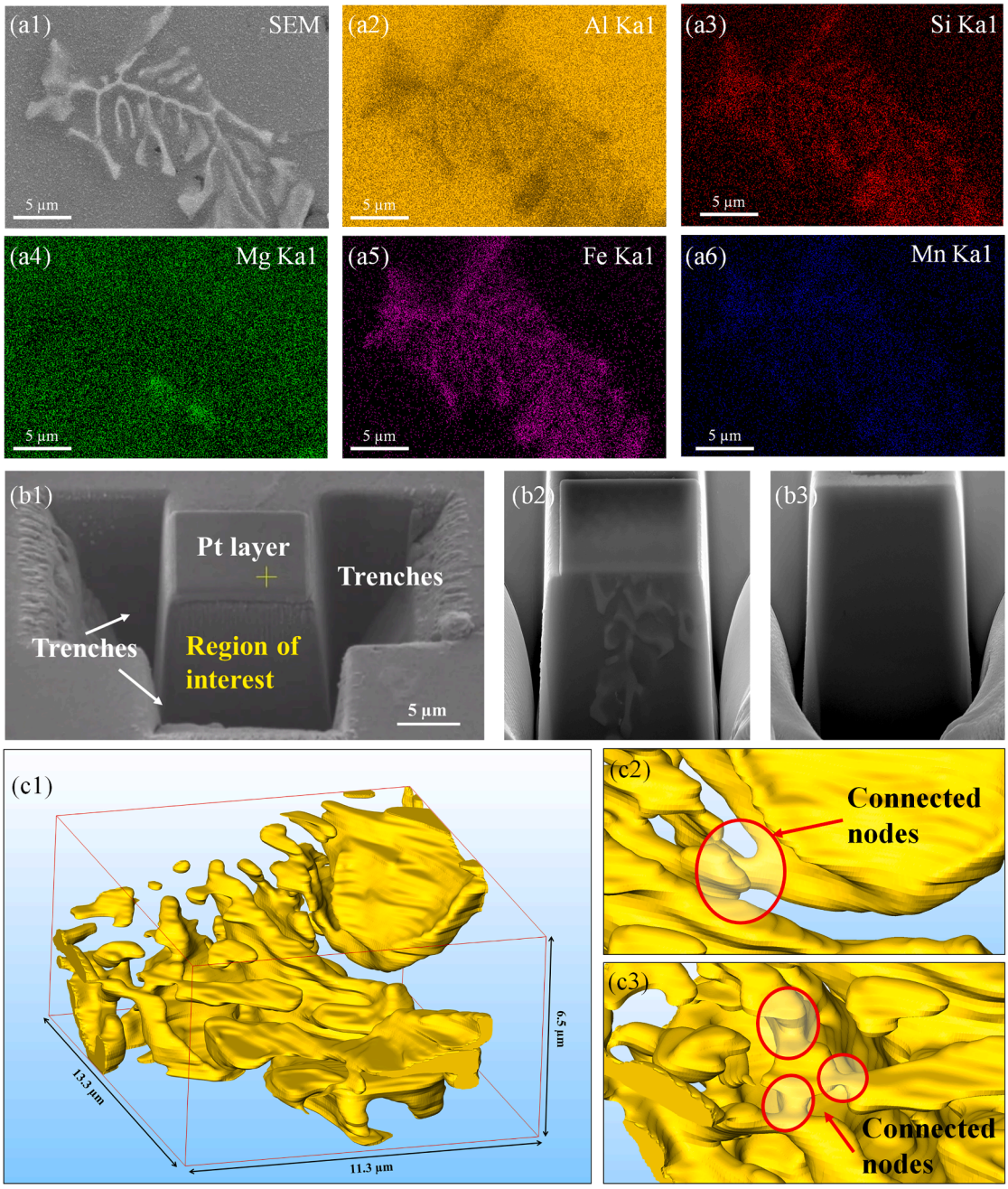

Fig. 10. (a1) The SEM image of Chinese-script α-AlFeMnSi phase and EDS elemental maps for (a2) Al, (a3) Si, (a4) Mg, (a5) Fe and (a6) Mn; SEM images of (b1) the ROI before sample milling and the (b2) first slice and (b3) last slice during milling; (c1) the reconstructed 3D morphology of the α-AlFeMnSi phase and (c2)(c3) connected nodes in detail.

nucleation, concurrent growth, and interconnection of multiple α-AlFeMnSi phases in inter dendritic regions, ultimately forming the characteristic convoluted structure.

(4) A rigorously physics-based predictive framework was established for the morphology evolution of Fe-contained IMCs. This methodology begins with first-principles calculations of interfacial energies based on the crystal structures. The obtained anisotropic interfacial energies are then incorporated into phase field models to simulate the morphology and formation process. Combined with high-throughput computational screening, this approach enables accurate prediction of the 3D morphology and formation process of Fe-contained IMCs modified by specific alloying elements, thereby identifying morphologically favorable Fe-contained IMCs and screening effective modifying elements. This study explores a way to transition from empirical trial-and-error methods to a rapid and design-oriented tool for developing morphology control strategies, supporting current efforts to mitigate the detrimental effect of Fe in Al alloys.

CRediT authorship contribution statement

Jiale Ma: Writing – original draft, Software, Methodology, Investigation, Formal analysis, Data curation. **Yanli Zhang:** Data curation. **Qing Peng:** Software, Resources. **Qingyan Xu:** Project administration. **Haidong Zhao:** Project administration. **Zhiqiang Han:** Writing – review & editing, Supervision, Project administration, Conceptualization.

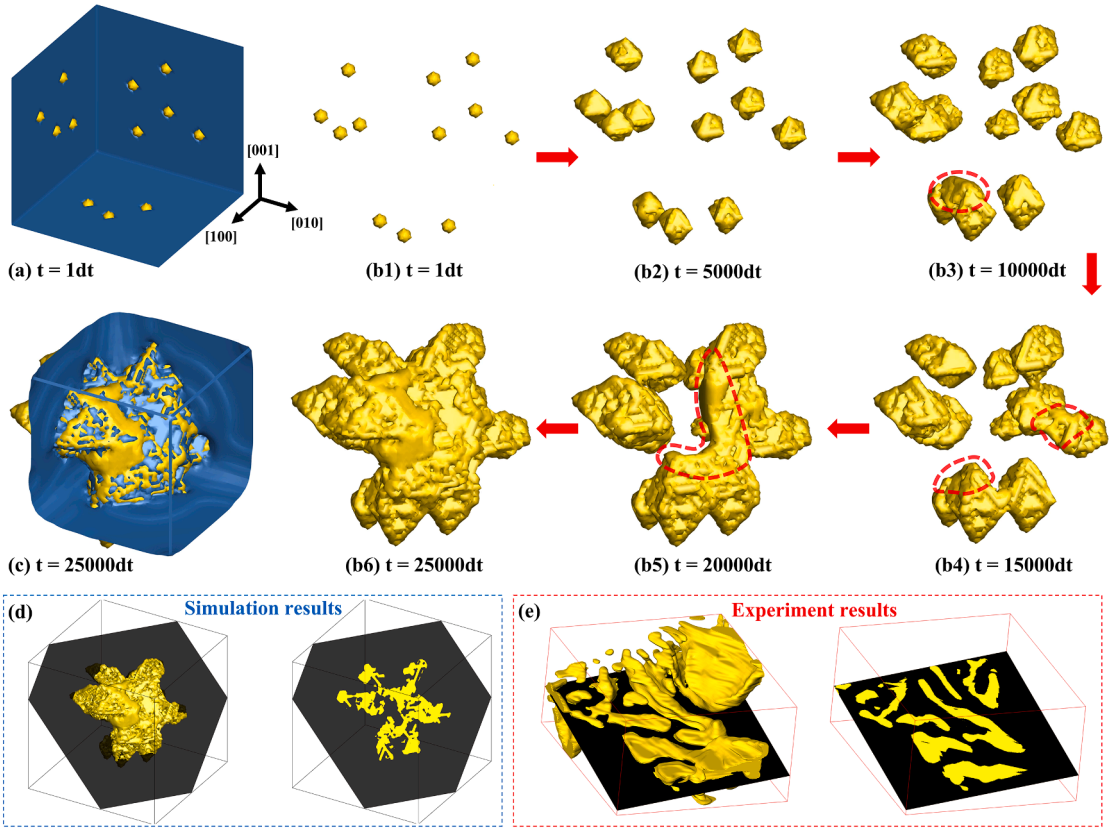

Fig. 11. The results for the formation process of Chinese-script α-AlFeMnSi phase: (a) α-AlFeMnSi nuclei (yellow) and Al phases (blue) at 1dt; (b1)-(b6) morphology evolution of α-AlFeMnSi phase; (c) α-AlFeMnSi phase (yellow) and Al phases (blue) at 25,000 dt; (d) 2D slice of the 3D multiphase field simulation results and (e) 2D slice of the 3D FIB-SEM tomography results, where black represents the Al phase and yellow represents the α-AlFeMnSi phase.

Declaration of competing interest

The authors declare that they have no known competing financial interests or personal relationships that could have appeared to influence the work reported in this paper.

Acknowledgements

The work is funded by Beijing Natural Science Foundation (L223001), Tsinghua University - Toyota Research Center (20253930061), and Tsinghua University research project (20251670005).

Appendix A

In the phase field models, the total free energy F of the system is formulated as Eq. A.1.

$$F = \int_V \left(\frac{\varepsilon^2}{2} |\nabla \phi^2| + g(\phi) + h(\phi) f^S + [1 - h(\phi)] f^L \right) dV \tag{A.1}$$

$$f^\delta(c_{1\delta}, c_{2\delta}, c_{3\delta} \ldots) = G^\delta / V_M \qquad \delta = L, S \tag{A.2}$$

The chemical free energy density f^δ is described using a CALPHAD-based approach. For the FCC_Al and Liquid phases, the molar Gibbs free energy G^δ is constituted by the weighted sum of the free energies of the pure elements, the ideal mixing contribution, and the excess free energy, as described by the Redlich-Kister polynomial (Eq. A.3).

$$G^\delta = \sum_{i=1}^{m} c_i {}^0G_i^\delta + RT \sum_{i=1}^{m} c_i \ln c_i + \sum_{i=1}^{m-1} \sum_{j=i+1}^{m} c_i c_j L_{i,j}^\delta \tag{A.3}$$

where δ represents solid or liquid, R is the gas constant, T is the temperature, $L_{i,j}^\delta$ is interaction parameter, c_i and ${}^0G_i^\delta$ represent the mole fraction and the Gibbs free energy of the pure element i, respectively.

For the Fe-contained IMCs (such as π-AlFeMgSi (Eq. A.4), α-AlFeMnSi (Eq. A.5), and β-AlFeSi (Eq. A.6)), their Gibbs free energies were adopted from the literature [61–63], where these IMCs are treated as stoichiometric compounds within the CALPHAD framework.

$$\begin{aligned} G_{Al_9FeMg_3Si_5} = {} & (18/37)^0 G_{Al}^{Fcc\_Al} + (2/37)^0 G_{Fe}^{Bcc\_A2} + (7/37)^0 G_{Mg}^{Hcp\_A3} \\ & + (10/37)^0 G_{Si}^{Diamond\_A4} - 12959 + 1.54T \end{aligned} \tag{A.4}$$

$$G_{Al_8FeMnSi_2} = (16/23)^0G_{Al}^{Fcc\_Al} + (2/23)^0G_{Fe}^{Bcc\_A2} + (2/23)^0G_{Mn}^{cBcc\_A12} + (3/23)^0G_{Si}^{Diamond\_A4} - 17236 - 1.09865T \quad (A.5)$$

$$G_{Al_9Fe_2Si_2} = (9/13)^0G_{Al}^{Fcc\_Al} + (2/13)^0G_{Fe}^{Bcc\_A2} + (2/13)^0G_{Si}^{Diamond\_A4} - 19538.7 + 2.51768T \quad (A.6)$$

The thermodynamic parameters (Table A.1) for these phases were obtained from the Scientific Group Thermodata Europe (SGTE) database.

Table A.1
Thermodynamic model parameters and expressions of the Al-Mg-Si-Fe-Mn system.

Gibbs free energy ${}^0G_i^\delta$
Liquid phase
${}^0G_{Al}^{L} = \begin{cases} 298.15K \le T < 933.473K : 11005.045 - 11.84185T + 7.934\cdot10^{-20}T^7 + {}^0G_{Al}^{Fcc\_Al} \\ 933.473K \le T < 2900\ K : -795.991 + 177.4302T - 31.7482T\ln(T) \end{cases}$
${}^0G_{Mg}^{L} = \begin{cases} 298.15K \le T < 923\ K : 8202.243 - 8.83693T - 8.0176\cdot10^{-20}T^7 + {}^0G_{Mg}^{Hcp\_A3} \\ 923K \le T < 3000\ K : -5439.869 + 195.324057T - 34.3088T\ln(T) \end{cases}$
${}^0G_{Si}^{L} = \begin{cases} 298.15K \le T < 1687K : 50696.36 - 30.099439T + 2.09307\cdot10^{-20}T^7 + {}^0G_{Si}^{Diamond\_A4} \\ 1687K \le T < 3600\ K : 40370.523 + 137.722298T - 27.196T\ln(T) \end{cases}$
${}^0G_{Fe}^{L} = \begin{cases} 298.15K \le T < 1811\ K : 12040.17 - 6.55843T - 3.67516\cdot10^{-20}T^7 + {}^0G_{Fe}^{Bcc\_A2} \\ 1811K \le T < 6000\ K : -10838.83 + 291.302T - 46T\ln(T) \end{cases}$
${}^0G_{Mn}^{L} = \begin{cases} 298.15K \le T < 1519\ K : 17859.91 - 12.6208T - 441.929\cdot10^{-23}T^7 + {}^0G_{Mn}^{cBcc\_A12} \\ 1519K \le T < 2000\ K : -9993.9 + 299.036T - 48T\ln(T) \end{cases}$
Solid phase
${}^0G_{Al}^{Fcc\_Al} = \begin{cases} 298.15K \le T < 700K : -7976.15 + 137.093038T - 24.3671976T\ln(T) \\ -0.0018846627^2 - 0.877664\cdot10^{-6}T^3 + 74092T^{-1} \\ 700K \le T < 933.473K : -11276.24 + 223.048446T - 38.5844296T\ln(T) \\ +0.018531982T^2 - 5.764227\cdot10^{-6}T^3 + 74092T^{-1} \\ 933.473K \le T < 2900\ K : -11278.361 + 188.684136T - 31.748192T\ln(T) \\ -1.230622\cdot10^{28}T^{-9} \end{cases}$
${}^0G_{Fe}^{Bcc\_A2} = \begin{cases} 298.15K \le T < 1811K : 1225.7 + 124.134T - 23.5143T\ln(T) \\ -4.39752\cdot10^{-3}T^2 - 5.8927\cdot10^{-8}T^3 + 77359T^{-1} \\ 1811K \le T < 6000\ K : -25383.581 + 299.31255T - 46T\ln(T) \\ +2.29603\cdot10^{31}T^{-9} \end{cases}$
${}^0G_{Si}^{Diamond\_A4} = \begin{cases} 298.15K \le T < 1687K : -8162.609 + 137.236859T - 22.8317533T\ln(T) \\ -1.912904\cdot10^{-3}T^2 - 3.552\cdot10^{-9}T^3 + 176667T^{-1} \\ 1687K \le T < 3600\ K : -9457.642 + 167.281367T - 27.196T\ln(T) \\ -4.20369\cdot10^{31}T^{-9} \end{cases}$
${}^0G_{Mg}^{Hcp\_A3} = \begin{cases} 298.15K \le T < 923K : -8367.34 + 143.675547T - 26.1849782T\ln(T) \\ +0.4858\cdot10^{-3}T^2 - 1.393669\cdot10^{-6}T^3 + 78950T^{-1} \\ 923K \le T < 3000\ K : -14130.185 + 204.716215T - 34.3088T\ln(T) \\ +1038.192\cdot10^{25}T^{-9} \end{cases}$
${}^0G_{Mn}^{cBcc\_A12} = \begin{cases} 298.15K \le T < 1519K : -8115.28 + 130.059T - 23.4582T\ln(T) \\ -7.34768\cdot10^{-3}T^2 + 69827T^{-1} \\ 1519K \le T < 2000\ K : -28733.41 + 312.2648T - 48T\ln(T) \\ +1656.847\cdot10^{27}T^{-9} \end{cases}$
Interaction parameter $L_{i,j}^\delta$
Liquid phase
$L_{Al,Si}^{L} = -11340.1 - 1.23394T + (-3530.9 + 1.35993T)(x_{Al} - x_{Si})$
$L_{Al,Mg}^{L} = -9374.468 + 2.3082T + (470.2715 - 0.12679T)(x_{Al} - x_{Mg})$
$L_{Al,Fe}^{L} = -88090 + 19.8T + (-3800 + 3T)(x_{Al} - x_{Fe})$
$L_{Mg,Si}^{L} = -66985.2876 + 16.6774T + (-30504.9231 + 17.0716T)(x_{Mg} - x_{Si})$
$L_{Fe,Mg}^{L} = 61343 + 1.5T - 2700(x_{Fe} - x_{Mg})$
$L_{Fe,Si}^{L} = -164434.6 + 41.9773T - 21.523T(x_{Fe} - x_{Si})$
Solid phase (FCC_Al)
$L_{Al,Si}^{Fcc\_Al} = -3143.78 - 0.39T$
$L_{Al,Mg}^{Fcc\_Al} = 2803.66 + 0.52T + (-280.75 + 0.54T)(x_{Al} - x_{Mg})$
$L_{Al,Fe}^{Fcc\_Al} = -104700 + 30.65T + (30000 - 7T)(x_{Al} - x_{Fe}) + (32200 - 17T)(x_{Al} - x_{Fe})^2$
$L_{Fe,Si}^{Fcc\_Al} = -115254.05 - 2.19T + (-84776.91 + 44.33T)(x_{Fe} - x_{Si}) + 20007.03(x_{Fe} - x_{Si})^2$
$L_{Mg,Si}^{Fcc\_Al} = -7148.79 + 0.89T$
$L_{Fe,Mg}^{Fcc\_Al} = 6938.398$

References

[1] G. Liu, D.B. Müller, Centennial evolution of aluminum in-use stocks on our aluminized planet, Environ. Sci. Technol. 47 (2013) 4882–4888.
[2] R.G. Billy, D.B. Müller, Aluminium use in passenger cars poses systemic challenges for recycling and GHG emissions, Resour. Conserv. Recycl. 190 (2023) 106827.
[3] H.W.L. Phillips, Annotated Equilibrium Diagrams of Some Aluminium Alloy Systems, The Institute of Metals, London, 1959.
[4] Z. Li, N. Limodin, A. Tandjaoui, P. Quaegebeur, J.F. Witz, D. Balloy, Influence of Fe content on the damage mechanism in A319 aluminum alloy: tensile tests and digital image correlation, Eng. Fract. Mech. 183 (2017) 94–108.
[5] I. Bacaicoa, M. Luetje, M. Wicke, A. Geisert, F. Zeismann, M. Fehlbier, A. Brueckner-Foit, 3D Morphology of Al5FeSi inclusions in high Fe-content Al-Si-Cu alloys, Procedia Structural Integrity 2 (2016) 2269–2276.
[6] J.Z. Yi, Y.X. Gao, P.D. Lee, T.C. Lindley, Effect of Fe-content on fatigue crack initiation and propagation in a cast aluminum–silicon alloy (A356–T6), Mater. Sci. Eng. A 386 (2004) 396–407.
[7] L. Zhang, J. Gao, L.N.W. Damoah, D.G. Robertson, Removal of iron from aluminum: a review, Min. Proc. Ext. Met. Rev. 33 (2012) 99–157.
[8] B. Sun, N. Sun, L. Wang, Y. Li, Z. Guo, Efficient purification of scrap 1060 aluminum alloys contaminated with Fe and Si by super-gravity separation, Process Saf. Environ. 177 (2023) 486–495.
[9] Q. Tang, J.H. Zhao, T. Wang, J. Chen, K. He, The effects of neodymium addition on the intermetallic microstructure and mechanical properties of Al-7Si-0.3Mg-0.3Fe alloys, J. Alloys Compd. 741 (2018) 161–173.
[10] M. Wang, W. Xu, Q.Y. Han, Study of refinement and morphology change of AlFeSi phase in A380 alloy due to addition of Ca, Sr/Ca, Mn and Mn, Sr, Mater. Trans. 57 (2016) 1509–1513.
[11] R. Oliveira, R. Kakitani, L.R. Ramos, D.L. Gonçalves, A. Garcia, N. Cheung, The roles of Mn and Ni additions to Fe-contaminated Al in neutralizing Fe and stabilizing the cellular α-Al microstructure, J. Sustain. Metall. 5 (2019) 561–580.
[12] B. Lin, H.Y. Li, R. Xu, H.Q. Xiao, W.W. Zhang, S.B. Li, Effects of vanadium on modification of iron-rich intermetallics and mechanical properties in A356 cast alloys with 1.5wt.% Fe, J. Mater. Eng. Perform. 28 (2019) 475–484.
[13] J. Santos, A.E.W. Jarfors, A.K. Dahle, Formation of iron-rich intermetallic phases in Al-7Si-Mg: influence of cooling rate and strontium modification, Metall. Mater. Trans. A 50 (2019) 4148–4165.
[14] H. Saghafian, S.G. Shabestari, S. Ghadami, M.H. Ghoncheh, Effects of iron, manganese, and cooling rate on microstructure and dry sliding wear behavior of LM13 aluminum alloy, Tribol. T. 60 (2017) 888–901.
[15] M.P. Moodispaw, J.S. Miao, E. Cinkilic, A.A. luo, The beneficial effect of Ce additions to high Fe-containing secondary Al-Si-Mg cast alloys, J. Alloys Compd. 1009 (2024) 176864.
[16] Y.C. Tzeng, S.Y. Jian, Effects of the addition of trace amounts of *Sc* on the microstructure and mechanical properties of Al-11.6Si alloys, Mat. Sci. Eng. A 723 (2018) 22–28.
[17] Y.L. Liu, L. Luo, C.F. Han, L.Y. Ou, J.J. Wang, C.Z. Liu, Effect of Fe, Si and cooling rate on the formation of Fe-and Mn-rich intermetallics in Al-5Mg-0.8Mn alloy, J. Mater. Sci. Technol. 32 (2016) 305–312.
[18] M.E. Farina, P. Bell, C.R.F. Ferreira, B.A. Dedavid, Effects of solidification rate in the microstructure of Al-Si5Cu3 aluminum cast alloy, Mater. Res. 20 (2017) 273–278.
[19] J.Y. Yao, J.A. Taylor, Characterisation of intermetallic particles formed during solution treatment of an Al-7Si-0.4 Mg-0.12 Fe alloy, J. Alloys Compd. 519 (2012) 60–66.
[20] E.A. Elsharkawi, E. Samuel, A.M. Samuel, F.H. Samuel, Effects of Mg, Fe, Be additions and solution heat treatment on the π-AlMgFeSi iron intermetallic phase in Al-7Si-Mg alloys, J. Mater. Sci. 45 (2010) 1528–1539.
[21] W.W. Zhang, B. Lin, Z. Luo, Y.L. Zhao, Y.Y. Li, Formation of Fe-rich intermetallic compounds and their effect on the tensile properties of squeeze-cast Al-Cu alloys, J. Mater. Res. 30 (2015) 2474–2484.
[22] D.G. Eskin, I. Tzanakis, F. Wang, G.S.B. Lebon, T. Subroto, K. Pericleous, J. Mi, Fundamental studies of ultrasonic melt processing, Ultrason. Sonochem. 52 (2019) 455–467.
[23] E. Cinkilic, M. Moodispaw, J. Zhang, J. Miao, A.A. Luo, A new recycled Al–Si–Mg alloy for sustainable structural die casting applications, Metall. Mater. Trans. A. 53 (2022) 2861–2873.
[24] E. Cinkilic, C.D. Ridgeway, X. Yan, A.A. Luo, A formation map of iron-containing intermetallic phases in recycled cast aluminum alloys, Metall. Mater. Trans. A 50 (2019) 5945–5956.
[25] D. Bösch, S. Pogatscher, M. Hummel, W. Fragner, P.J. Uggowitzer, M. Göken, H. W. Höppel, Secondary Al-Si-Mg high-pressure die cast alloys with enhanced ductility, Metall. Mater. Trans. A 46 (2015) 1035–1045.
[26] S. Seifeddine, S. Johansson, I.L. Svensson, The influence of cooling rate and manganese content on the β-Al5FeSi phase formation and mechanical properties of Al–Si-based alloys, Mat. Sci. Eng. A 490 (2008) 385–390.
[27] J.Z. Yi, Y.X. Gao, P.D. Lee, T.C. Lindley, Effect of Fe-content on fatigue crack initiation and propagation in a cast aluminum-silicon alloy (A356-T6), Mat. Sci. Eng. A 386 (2004) 396–407.
[28] D.T. Wang, X.Z. Zhang, H. Nagaumi, M.H. Zhang, P.F. Zhou, R. Wang, B. Zhang, Exploring the relationship between the structural characteristics and mechanical behavior of multicomponent Fe-containing phases: experimental studies and first-principles calculations, Molecules 28 (2023) 7141.
[29] S. Terzi, J.A. Taylor, Y.H. Cho, L. Salvo, M. Suéry, E. Boller, A.K. Dahle, In situ study of nucleation and growth of the irregular α-Al/β-Al5FeSi eutectic by 3-D synchrotron X-ray microtomography, Acta Mater. 58 (2010) 5370–5380.
[30] T. Gao, Y.Y. Wu, C. Li, X.F. Liu, Morphologies and growth mechanisms of α-Al (FeMn)Si in Al–Si–Fe–Mn alloy, Mater. Lett. 110 (2013) 191–194.
[31] A. Bjurenstedt, D. Casari, S. Seifeddine, R.H. Mathiesen, A.K. Dahle, In-situ study of morphology and growth of primary α-Al(FeMnCr)Si intermetallics in an Al-Si alloy, Acta Mater. 130 (2017) 1–9.
[32] X.Y. Jiao, C.F. Liu, Z.P. Guo, H. Nishat, G.D. Tong, S.L. Ma, Y. Bi, Y.F. Zhang, S. Wiesner, S.M. Xiong, On the characterization of primary iron-rich phase in a high-pressure die-cast hypoeutectic Al-Si alloy, J. Alloys Compd. 862 (2021) 158580.
[33] X.L. Wang, H.D. Zhao, Q.Y. Xu, Z.Q. Han, Clustering characteristics of Fe-rich intermetallics in high vacuum die cast AlSiMgMn alloys with high resolution μ-CT inspection, Mater. Charact. 207 (2024) 113607.
[34] F. Schmidt, M. Kühbacher, U. Gross, A. Kyriakopoulos, H. Schubert, R. Zehbe, From 2D slices to 3D volumes: image based reconstruction and morphological characterization of hippocampal cells on charged and uncharged surfaces using FIB/SEM serial sectioning, Ultramicroscopy 111 (2011) 259–266.
[35] L.M. Keller, L. Holzer, R. Wepf, P. Gasser, 3D geometry and topology of pore pathways in Opalinus clay: implications for mass transport, Appl. Clay. Sci. 52 (2011) 85–95.
[36] G. Neusser, S. Eppler, J. Bowen, C.J. Allender, P. Walther, B. Mizaikoff, C. Kranz, FIB and MIP: understanding nanoscale porosity in molecularly imprinted polymers via 3D FIB/SEM tomography, Nanoscale 38 (2017) 14327–14334.
[37] K.X. Chen, G. Demange, X. Cui, Z.D. Wang, X.L. Pang, R. Patte, H.H. Mao, X. H. Chen, R.J. Shi, H. Zapolsky, 3D morphology of the petal-like precipitates in Cu-Fe alloys: experimental study and phase field modelling, Acta Mater. 270 (2024) 119874.
[38] Y.H. Zhao, Understanding and design of metallic alloys guided by phase-field simulations, npj Comput. Mater. 9 (2023) 94.
[39] Y.H. Zhao, Editorial: phase field method and integrated computing materials engineering, Front. Mater. 10 (2023) 1145833.
[40] W.H. Ning, W.D. Zhang, Y.H. Zhao, Phase-field simulation for evolution of iron-rich phase during solidification of Al–Si–Fe alloys, J. Mater. Res. Technol. 29 (2024) 5495–5506.
[41] M.B. Amar, E. Brener, Theory of pattern selection in three-dimensional nonaxisymmetric dendritic growth, Phys. Rev. Lett. 71 (1993) 589–592.
[42] Y.H. Zhao, K. Liu, H. Hou, L.Q. Chen, Role of interfacial energy anisotropy in dendrite orientation in Al-Zn alloys: a phase field study, Mater. Des. 216 (2022) 110555.
[43] L. Wang, J.J. Hoyt, N. Wang, N. Provatas, C.W. Sinclair, Controlling solid-liquid interfacial energy anisotropy through the isotropic liquid, Nat. Commun. 724 (2020) 11.
[44] M.E. Glicksman, N.B. Singh, Effects of crystal-melt interfacial energy anisotropy on dendritic morphology and growth kinetics, J. Cryst. Growth 98 (1989) 277–284.
[45] S. Liu, R.E. Napolitano, R. Trivedi, Measurement of anisotropy of crystal-melt interfacial energy for a binary Al–Cu alloy, Acta Mater. 49 (2001) 4271–4276.
[46] R.E. Napolitano, S. Liu, R. Trivedi, Experimental measurement of anisotropy in crystal-melt interfacial energy, Interface Sci. 10 (2002) 217–232.
[47] R.E. Rozas, J.L. Orrego, P.G. Toledo, Interfacial properties and crystal growth of Ni and Ni50Al50 from molecular dynamics simulations, J. Appl. Phys. 133 (2023) 214701.
[48] D.Y. Sun, M.I. Mendelev, C.A. Becker, K. Kudin, T. Haxhimali, M. Asta, J.J. Hoyt, A. Karma, D.J. Srolovitz, Crystal-melt interfacial free energies in hcp metals: a molecular dynamics study of Mg, Phys. Rev. B 73 (2006) 024116.
[49] R. Yan, S.D. Ma, W.Z. Sun, T. Jing, H.B. Dong, The solid–liquid interface free energy of Al: a comparison between molecular dynamics calculations and experimental measurements, Comp. Mater. Sci. 184 (2020) 109910.
[50] X.Z. Zhang, D.T. Wang, H. Nagaumi, R. Wang, Z.B. Wu, M.H. Zhang, D.S. Gao, H. Chen, P.F. Wang, P.F. Zhou, Y.X. Zhou, Z.X. Wang, T.L. Li, Accelerating the design of highly separable Fe-containing intermetallics in Al–Si alloys via DFT calculations and experimental validation, MGE Adv. 3 (2025) e7008.
[51] T. Auger, L.L. Wang, D.D. Johnson, X. Gong, First-principles study of grain-boundary wetting in Fe-Σ5(013)[100]tilt boundary, Acta Mater. 265 (2024) 119635.
[52] P.E. Blöchl, Projector augmented-wave method, Phys. Rev. B 50 (1994) 17953.
[53] G. Kresse, J. Furthmüller, Efficiency of ab-initio total energy calculations for metals and semiconductors using a plane-wave basis set, Comput. Mater. Sci. 6 (1996) 15–50.
[54] M. Methfessel, A.T. Paxton, High-precision sampling for Brillouin-zone integration in metals, Phys. Rev. B 40 (1989) 3616.
[55] A.P. Thompson, H.M. Aktulga, R. Berger, D.S. Bolintineanu, W.M. Brown, P. S. Crozier, P.J. Veld, A. Kohlmeyer, S.G. Moore, T.D. Nguyen, R. Shan, M. J. Stevens, J. Tranchida, C. Trott, S.J. Plimpton, LAMMPS-a flexible simulation tool for particle-based materials modeling at the atomic, meso, and continuum scales, Comput. Phys. Commun. 271 (2022) 108171.
[56] M.I. Mendelev, M.J. Kramer, C.A. Becker, M. Asta, Analysis of semi-empirical interatomic potentials appropriate for simulation of crystalline and liquid Al and Cu, Phil. Mag. 88 (2008) 1723–1750.
[57] M.I. Mendelev, M. Asta, M.J. Rahman, J.J. Hoyt, Development of interatomic potentials appropriate for simulation of solid-liquid interface properties in Al-Mg alloys, Phi. Mag. 89 (2009) 3269–3285.
[58] C.A. Becker, M.J. Kramer, Atomistic comparison of volume-dependent melt properties from four models of aluminum, Modelling Simul. Mater. Sci. Eng. 18 (2010) 074001.
[59] A. Karma, W.J. Rappel, Numerical simulation of three-dimensional dendritic growth, Phys. Rev. Lett. 77 (1996) 4050–4053.

[60] A. Karma, W.J. Rappel, Quantitative phase-field modeling of dendritic growth in two and three dimensions, Phys. Rev. E 57 (1998) 4323–4349.
[61] Y. Du, J.C. Schuster, Z.K. Liu, R.X. Hu, P. Nash, W.H. Sun, W.W. Zhang, J. Wang, L. J. Zhang, C.Y. Tang, Z.J. Zhu, S.H. Liu, Y.F. Ouyang, W.Q. Zhang, N. Krendelsberger, A thermodynamic description of the Al-Fe-Si system over the whole composition and temperature ranges via a hybrid approach of CALPHAD and key experiments, Intermetallics 16 (2008) 554–570.
[62] Y. Du, Y.A. Chang, S.H. Liu, B.Y. Huang, F.Y. Xie, Y. Yang, S.L. Chen, Thermodynamic description of the Al–Fe–Mg–Mn–Si system and investigation of microstructure and microsegregation during directional solidification of an Al–Fe–Mg–Mn–Si alloy, Z. Metallkd. 96 (2005) 1351–1362.
[63] B. Hu, S. Qin, Y. Du, Z.Y. Li, Q.P. Wang, Thermodynamic description of the Al-Fe-Mg-Ni-Si and Al-Cu-Fe-Mg-Ni quinary systems and its application to solidification simulation, J. Phase Equilib. Diffus. 36 (2015) 333–349.
[64] M. Ode, J.S. Lee, S.G. Kim, W.T. Kim, T. Suzuki, Phase-field model for solidification of ternary alloys, ISIJ Int. 40 (2000) 870–876.
[65] S.G. Kim, W.T. Kim, T. Suzuki, T. Suzuki, M. Ode, Phase-field modeling of eutectic solidification, J. Cryst. Growth 261 (2004) 135–158.
[66] H.H. Xi, J.J. Xu, X. Yuan, W.Q. Ming, Z. Zhang, J.H. Chen, The ill-defined π(AlFeMgSi) phase intermetallics formed in an automotive Al-Si-Mg alloy, Mater. Charact. 199 (2023) 112839.
[67] G. Davignon, B. Verlinden, L. Delaey, A. Serneels, An isothermal section at 550 °C in the Al-Rich corner of the Al-Fe-Mn-Si system; precipitation of α-Al(Fe,Mn)Si from the melt, Metall. Mater. Trans. A 27 (1996) 3357–3361.
[68] M. Warmuzek, Primary crystals of AlFeMnSi intermetallics in the cast AlSi alloys, Arch. Metall. Mater. 62 (2017) 1659–1664.
[69] T. Gao, K.Q. Hu, L.S. Wang, B.G. Zhang, X.F. Liu, Morphological evolution and strengthening behavior of α-Al(Fe,Mn)Si in Al–6Si–2Fe–xMn alloys, Results Phys. 7 (2017) 1051–1054.
[70] A. Dinsdale, C. Fang, Z. Que, Z.Y. Fan, Understanding the thermodynamics and crystal structure of complex Fe containing intermetallic phases formed on solidification of aluminium alloys, JOM 71 (2019) 1731–1736.
[71] X.Z. Zhang, D.T. Wang, H. Nagaumi, Y.X. Zhou, W. Yu, X.Y. Chong, X.Z. Li, H. T. Zhang, Morphology, thermal stability, electronic structure and mechanical properties of α-AlFeMnSi phases with varying Mn/Fe atomic ratios: experimental studies and DFT calculations, J. Alloys Compd. 901 (2022) 163523.
[72] X.Z. Zhang, D.T. Wang, X.Z. Li, H.T. Zhang, H. Nagaumi, Understanding crystal structure and morphology evolution of Fe, Mn, Cr-containing phases in Al-Si cast alloy, Intermetallics 131 (2021) 107103.
[73] C.M. Fang, Z.P. Que, Z. Fan, Crystal chemistry and electronic structure of the β-AlFeSi phase from first-principles, J. Solid State Chem. 299 (2021) 122199.
[74] G.J. Carpenter, Y. Lepage, Revised cell data for the SiAl phase in aluminum alloys, Scripta Metall. Mater. 28 (1993) 733–736.
[75] C. Rømming, V. Hansen, J. Gjønnes, Crystal structure of β-Al4.5FeSi, Acta Crystallogr. B50 (1994) 307–312.
[76] J.G. Zheng, R. Vincent, J.W. Steeds, Crystal structure of an orthorhombic phase in β-(Al-Fe-Si) precipitates determined by convergent-beam electron diffraction, Philos. Mag. A 80 (2000) 493–500.
[77] C.A. Becker, M.J. Kramer, Atomistic comparison of volume-dependent melt properties from four models of aluminum, Modelling Simul. Mater. Sci. Eng. 18 (2010) 074001.
[78] K.J. Smolander, Monte Carlo study of aluminium in liquid and amorphous states, Phys. Scr. 31 (1985) 427–432.
[79] Z.G. Xia, D.Y. Sun, M. Asta, J.J. Hoyt, Molecular dynamics calculations of the crystal-melt interfacial mobility for hexagonal close-packed Mg, Phys. Rev. B 75 (2007) 012103.
[80] W.R. Fehlner, S.H. Vosko, A product representation for cubic harmonics and special directions for the determination of the Fermi surface and related properties, Can. J. Phys. 54 (1976) 2159–2169.
[81] R. Tran, Z. Xu, B. Radhakrishnan, D. Winston, W. Sun, K. Persson, S. Ping, Surface energies of elemental crystals, Sci. Data 3 (2016) 160080.
[82] X. Liu, C. Wang, S.Y. Zhang, J.W. Song, X.L. Zhou, M. Zha, H.Y. Wang, Fe-bearing phase formation, microstructure evolution, and mechanical properties of Al-Mg-Si-Fe alloy fabricated by the twin-roll casting process, J. Alloys Compd. 886 (2021) 161202.
[83] M.X. Zhang, H. Ning, C. Wang, K. Guan, X. Wang, Z.G. Li, H.Y. Wang, Effectively mitigated macro-segregation and improved tensile properties of twin-roll cast Al–Mg–Si (6022) alloy strips via Zr addition, Mater. Sci. Eng. A 880 (2023) 145318.
[84] X. Liu, H.L. Jia, C. Wang, X. Wu, M. Zha, H.Y. Wang, Enhancing mechanical properties of twin-roll cast Al–Mg–Si–Fe alloys by regulating Fe-bearing phases and macro-segregation, Mater. Sci. Eng. A 831 (2022) 142256.
[85] X.Z. Zhang, D.T. Wang, Y.X. Zhou, X.Y. Chong, X.Z. Li, H.T. Zhang, H. Nagaumi, Exploring crystal structures, stability and mechanical properties of Fe, Mn-containing intermetallics in Al-Si Alloy by experiments and first-principles calculations, J. Alloys Compd. 876 (2021) 160022.
[86] K. Xiang, L. Qin, Y.L. Zhao, S. Huang, W.J. Du, E. Boller, A. Rack, M. Li, J. Mi, Operando study of the dynamic evolution of multiple Fe-rich intermetallics of an Al recycled alloy in solidification by synchrotron X-ray and machine learning, Acta Mater. 279 (2024) 120267.
[87] X.Z. Zhang, D.T. Wang, H. Nagaumi, Z.B. Wu, M.H. Zhang, R. Wang, J. Zou, H. Chen, P.F. Wang, P.F. Zhou, Unveiling the growth mechanism of Fe-containing intermetallics in Al–Si alloy in the perspective of surface stability and atom adsorption, J. Mater. Res. Technol. 35 (2025) 2458–2470.
[88] C. Puncreobutr, A.B. Phillion, J.L. Fife, P. Rockett, A.P. Horsfield, P.D. Lee, In situ quantification of the nucleation and growth of Fe-rich intermetallics during Al alloy solidification, Acta Mater. 79 (2014) 292–303.
[89] Z. Que, Y. Wang, C.L. Mendis, C. Fang, J. Xia, X. Zhou, Z. Fan, Understanding Fe-containing intermetallic compounds in Al alloys: an overview of recent advances from the LiME Research Hub, Metals 12 (2022) 1677.
[90] S. Feng, M. Shearwood, A. Lui, D. Banks, T. Nicholls, S. Richards, M.D. Wilson, P. S. Grant, E. Liotti, Probing the mechanisms of morphological evolution and phase selection of intermetallic compounds for impurity-tolerant processing of recycled Al alloys, Acta Mater. 301 (2025) 121591.